
BiLO: Bilevel Local Operator Learning for PDE inverse problems

Ray Zirui Zhang¹ Xiaohui Xie² John S. Lowengrub^{1,3}

Abstract

We propose a new neural network based method for solving inverse problems for partial differential equations (PDEs) by formulating the PDE inverse problem as a bilevel optimization problem. At the upper level, we minimize the data loss with respect to the PDE parameters. At the lower level, we train a neural network to locally approximate the PDE solution operator in the neighborhood of a given set of PDE parameters, which enables an accurate approximation of the descent direction for the upper level optimization problem. The lower level loss function includes the L2 norms of both the residual and its derivative with respect to the PDE parameters. We apply gradient descent simultaneously on both the upper and lower level optimization problems, leading to an effective and fast algorithm. The method, which we refer to as BiLO (Bilevel Local Operator learning), is also able to efficiently infer unknown functions in the PDEs through the introduction of an auxiliary variable. Through extensive experiments over multiple PDE systems, we demonstrate that our method enforces strong PDE constraints, is robust to sparse and noisy data, and eliminates the need to balance the residual and the data loss, which is inherent to the soft PDE constraints in many existing methods.

1. Introduction

A fundamental task across various scientific and engineering fields is to infer the unknown parameters of a partial differential equation (PDE) from observed data. Applications include seismic imaging (Deng et al., 2023; Martin et al., 2012; Yang et al., 2021b), electrical impedance to-

mography (Uhlmann, 2009; Molinaro et al., 2023), personalized medicine (Lipková et al., 2019; Zhang et al., 2024a; Schäfer et al., 2021; Subramanian et al., 2023), and climate modeling (Sen & Stoffa, 2013). PDE inverse problems are commonly addressed within the frameworks of PDE-constrained optimization (Hinze et al., 2008) or Bayesian inference (Stuart, 2010). In the PDE constrained optimization framework, the objective is to minimize the difference between the observed data and the PDE solution, and the PDE is enforced as a constraint using adjoint or deep learning methods. In the Bayesian inference framework, the inverse problem is formulated as a statistical inference problem, where the goal is to estimate the posterior distribution of the parameters given the data. This requires sampling parameter space and solving the forward PDE multiple times. Here, we develop a constrained optimization framework for solving PDE inverse problems using deep learning.

1.1. Related work

The **Adjoint Method** is a widely used technique for computing the gradients of the objective function with respect to the PDE parameters using numerical PDE solvers in the PDE-constrained optimization framework. This method provides accurate gradients and strong PDE constraint. However, the method requires explicitly deriving the adjoint equation and solving both forward and adjoint equations at each iteration, which is complex and computationally expensive, especially for nonlinear or high-dimensional problems (Hinze et al., 2008; Plessix, 2006).

Physics-Informed Neural Networks (PINNs) have emerged as novel methods for solving inverse problems in a PDE constrained optimization framework (Karniadakis et al., 2021; Raissi et al., 2019; Jagtap et al., 2022b;a; Chen et al., 2020; Zhang et al., 2024a; Yang et al., 2021a; Kapoor et al., 2024; Chen et al., 2020; Jagtap et al., 2022a; Zhang et al., 2024a). PINNs represent PDE solutions using neural networks and embed both the data and the PDE into the loss function through a mesh-free approach. By minimizing the total loss, PINNs effectively solve the PDE, fit the data, and infer the parameters simultaneously, showcasing integration of mathematical models with data-driven learning processes. A related approach, **Optimizing a Discrete Loss (ODIL)**, utilizes conventional numerical discretizations of

¹Department of Mathematics, University of California, Irvine
²Department of Computer Science, University of California, Irvine
³Department of Biomedical Engineering, University of California, Irvine. Correspondence to: Ray Zirui Zhang <zirui.zhang@uci.edu>.

the PDEs and the loss is minimized over the parameters and the PDE solutions at the grid points rather than the weights of a neural network (Karnakov et al., 2022; Balcerak et al., 2024). However, in these methods, the PDE is enforced as a soft constraint, which requires balancing the residual and the data loss, and can lead to a trade-off between fitting the data and solving the PDE accurately.

Neural Operators (NOs) aim to approximate the PDE solution operator (parameter-to-solution map) and can serve as surrogate models for the forward PDE solvers (Kovachki et al., 2022). Once these surrogates are established, they can be integrated into a Bayesian inference framework or other optimization algorithms to solve inverse problems, leveraging the speed of evaluating a neural network (Zhou et al., 2024; Pathak et al., 2022; Lu et al., 2022b; Mao et al., 2023). Some examples of operator learning frameworks include the Fourier Neural Operator (Li et al., 2021; 2024; White et al., 2023), DeepONet (Lu et al., 2021a; Wang et al., 2021b), In-context operator learning (Yang et al., 2023a), among others, e.g. (O’Leary-Roseberry et al., 2024; Molinaro et al., 2023). However, for solving the inverse problem, neural operators can encounter challenges when the ground truth is out of the distribution of the training dataset.

There are many other methods for PDE inverse problems using deep learning; see (Nganyu Tanyu et al., 2023; Herrmann & Kollmannsberger, 2024; Brunton & Kutz, 2023) for more comprehensive reviews.

Main Contributions

In this work, we focus on solving PDE inverse problems in the PDE-constrained optimization framework using deep learning methods. The contributions are as follows:

- We formulate the PDE inverse problem as a bilevel optimization problem, where the upper level problem minimizes the data loss with respect to the PDE parameters, and the lower level problem involves training a neural network to approximate the PDE solution operator locally at given PDE parameters, enabling direct computation of the descent direction for the upper level optimization problem.
- At the lower level problem, we introduce the “residual-gradient” loss, which is the L2 norm of derivative of the residual with respect to the PDE parameters. We show that this loss term compels the neural network to approximate the PDE solution for a small neighborhood of the PDE parameters, thus a “local operator”.
- Extensive experiments over multiple PDE systems demonstrate that our novel formulation is both more accurate and more robust than other existing methods. It

exhibits stronger PDE fidelity, robustness to sparse and noisy data, and eliminates the need to balance the residual and the data loss, a common issue in PDE-based soft constraints.

- We solve the bilevel optimization problem using gradient descent simultaneously on both the upper and lower level optimization problems, leading to an effective and fast algorithm. The network architecture is simple and easy to implement.
- We extend our method to infer unknown functions that are also parameterized by neural networks through an auxiliary variable. This bypasses the need to learn a high-dimensional local operator.

Our approach combines elements of PINN, operator learning, and the adjoint method. Our method is closely related to the PINN: both use neural network to represent the solution to the PDE, use automatic differentiation to compute the PDE residual, and aim to solve the PDE and infer the parameters simultaneously. However, in the PINN, the PDE-constraint is enforced as a regularization term (or soft constraint), leading to a trade-off between fitting the data and solving the PDE accurately. Compared with operator learning, which solves the PDE for a wide range of parameters and requires a large amount of synthetic data for training, our method only learns the operator local to the PDE parameters at each step of the optimization process and does not require a synthetic dataset for training. Similar to the adjoint method, we aim to approximate the descent direction for the PDE parameters with respect to the data loss, but we do not require deriving and solving the adjoint equation.

2. Method

2.1. PDE Inverse problem as Bi-level optimization

In this section, we present a novel method for solving PDE inverse problems in the framework of PDE-constrained optimization problems using deep learning. Let $u : \Omega \rightarrow \mathbb{R}$ be a function defined over a domain $\Omega \subset \mathbb{R}^d$ satisfying some boundary conditions, and \hat{u} be the observed data, which might be noisy. Suppose u is governed by a PDE, F , which depends on some parameters Θ . Then the following PDE-constrained optimization problem is solved:

$$\begin{aligned} \min_{\Theta} \quad & \|u - \hat{u}\|_2^2 \\ \text{s.t.} \quad & F(D^k u(\mathbf{x}), \dots, Du(\mathbf{x}), u(\mathbf{x}), \Theta) = 0 \end{aligned} \tag{1}$$

Fig. 1 illustrates the idea of our BiLO framework. Suppose we know the PDE solution operator (hereafter referred to as the “operator”), $u(\mathbf{x}, \Theta)$ (gray surface in Fig. 1), which

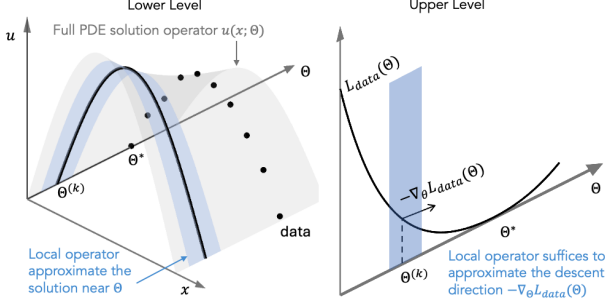


Figure 1: Schematics of BiLO: the full PDE operator $u(\mathbf{x}, \Theta)$ (gray) solves the PDE for all Θ , while the local operator (blue) approximates the solution in a small neighborhood of Θ . The local operator is sufficient for approximating the descent direction of the data loss. The figure uses the model PDE $-u_{xx} = \sin(\pi x)$

solves the PDE for any Θ , then we can solve the optimization problem easily by minimizing the objective function using a gradient descent algorithm. However, finding the full operator $u(\mathbf{x}, \Theta)$ is challenging and unnecessary. Since we are only interested in the descent direction to update Θ , a local approximation of the solution operator suffices (blue surface in Fig. 1), that is, the operator should approximate the PDE solution for a small neighborhood of a particular value of Θ .

For notational simplicity, we define the residual function of the operator as

$$r(\mathbf{x}, \Theta) := F(D^k u(\mathbf{x}, \Theta), \dots, Du(\mathbf{x}, \Theta), u(\mathbf{x}, \Theta), \Theta) \quad (2)$$

And the two defining properties of the local operator u are: (1) $r(\mathbf{x}, \Theta) = 0$, that u should solve the PDE at Θ , and (2) $\nabla_{\Theta} r(\mathbf{x}, \Theta) = 0$, which means that small variation of Θ should lead to small variation of the residual. If this is satisfied, then the derivative of the data loss with respect to Θ will approximate the descent direction, and we can find the optimal Θ by minimizing the data loss with respect to Θ using a gradient descent algorithm.

We will approximate the operator locally at Θ using a neural network. Suppose the local operator is parameterized by a neural network $u(\mathbf{x}, \Theta; W)$, where W are the weights of the network. The objective function (1) leads to the data loss:

$$\mathcal{L}_{\text{dat}}(\Theta, W) = \frac{1}{|\mathcal{T}_{\text{dat}}|} \sum_{\mathbf{x} \in \mathcal{T}_{\text{dat}}} |u(\mathbf{x}, \Theta; W) - \hat{u}(\mathbf{x})|^2, \quad (3)$$

where \mathcal{T}_{dat} is the set of collocation points for observed data. The residual loss is given by

$$\mathcal{L}_{\text{res}}(W, \Theta) := \frac{1}{|\mathcal{T}_{\text{res}}|} \sum_{\mathbf{x} \in \mathcal{T}_{\text{res}}} |r(\mathbf{x}, \Theta; W)|^2. \quad (4)$$

where \mathcal{T}_{res} is the set of collocation points for evaluating the residual. We introduce the following loss, the ‘‘residual-gradient loss’’, which is the L2 norm of the gradient of the residual with respect to Θ :

$$\mathcal{L}_{\text{rgrad}}(\Theta, W) = \frac{1}{|\mathcal{T}_{\text{res}}|} \sum_{\mathbf{x} \in \mathcal{T}_{\text{res}}} |\nabla_{\Theta} r(\mathbf{x}, \Theta)|^2. \quad (5)$$

We define the ‘‘local operator loss’’ as the sum of the residual loss and the residual-gradient loss with weight w_{rgrad} :

$$\mathcal{L}_{\text{LO}}(\Theta, W) = \mathcal{L}_{\text{res}}(\Theta, W) + w_{\text{rgrad}} \mathcal{L}_{\text{rgrad}}(\Theta, W) \quad (6)$$

Finally, we propose to solve the following bilevel optimization problem:

$$\begin{cases} \Theta^* = \arg \min_{\Theta} \mathcal{L}_{\text{dat}}(\Theta, W^*(\Theta)) \\ W^*(\Theta) = \arg \min_W \mathcal{L}_{\text{LO}}(\Theta, W) \end{cases} \quad (7)$$

In the upper level problem, we find the optimal PDE parameters Θ by minimizing the data loss with respect to Θ . In the lower level problem, we train a network to approximate the local operator $u(\mathbf{x}, \Theta; W)$ by minimizing the local operator loss with respect to the weights of the neural network.

Pre-train and Fine-tune Since the lower level problem need to be solved in order to obtain the decent direction for the upper level problem, we can pre-train the neural network to approximate the PDE solution operator at a given initial guess of the PDE parameters, Θ_0 . Subsequently, we can fine-tune the neural network using the data to infer the PDE parameters. The pretraining process can also be speed up if numerical solutions are available for the PDE at Θ_0 . This is computationally inexpensive as we only need one numerical solution.

Network Architecture The network architecture involves a simple modification at the input layer (embedding layer) of the typical fully connected neural network: the embedding of the PDE parameters Θ is randomly initialized and fixed during training, so that the residual-gradient loss can not be made 0 by setting the embedding to 0. See Appendix B for more details. The remaining layers of the neural network can be flexible.

2.2. Inferring an unknown function

We can also extend our method to learn an unknown function $f(\mathbf{x})$ in the PDE, such as a variable diffusion coefficient in the Poisson equation or an initial condition in the heat equation. In these cases, the following PDE constrained optimization problem is solved:

$$\begin{aligned} \min_f \quad & \|u - \hat{u}\|^2 + w_{\text{reg}} \|\nabla f\|^2 \\ \text{s.t.} \quad & F(D^k u(\mathbf{x}), \dots, Du(\mathbf{x}), u(\mathbf{x}), f(\mathbf{x})) = 0 \end{aligned} \quad (8)$$

where the constraint is a PDE that depends on the unknown function f . Given that these problems are ill-posed, regularization of the unknown function is often necessary. A typical choice is the L2-norm of the gradient of the unknown function, which penalizes non-smooth functions. While the selection of an appropriate regularization form is critical and depends on the PDE problem, this paper assumes such choices are predetermined, not an aspect of the method under direct consideration.

Suppose f is parameterized by a neural network $f(\mathbf{x}; V)$ with weights V . A straightforward extension from the scalar parameter case is to learn the local operator of the form $u(\mathbf{x}, V)$. However, this would be computationally expensive, as the weights V can be very high dimensional. We propose to introduce an auxiliary variable $z = f(\mathbf{x})$, and find a local operator $u(\mathbf{x}, z)$ such that $u(\mathbf{x}, f(\mathbf{x}))$ solves the PDE locally at f . We define the following function a , which is the residual function with an auxiliary variable z : $a(\mathbf{x}, z) := F(D^k u(\mathbf{x}, z), \dots, Du(\mathbf{x}, z), u(\mathbf{x}, z), z)$. If u is a local solution operator at f , then we should have: (1) $a(\mathbf{x}, f(\mathbf{x})) = 0$, that the function $u(\mathbf{x}, f(\mathbf{x}))$ have zero residual, and (2) $\nabla_z a(\mathbf{x}, f(\mathbf{x})) = 0$, that small variation of f should lead to small variation of the residual, which has the same interpretation as the parameter inference case (5). These two conditions translates to the corresponding residual loss and residual-gradient loss, similar to (4) and (5). The detailed definitions of the loss functions and the optimization problems are provided in Appendix A.

2.3. Algorithm

Solving a bilevel optimization problem is challenging in general (Zhang et al., 2023; Khanduri et al., 2023; Ye et al., 2022; Shen et al., 2023; Shaban et al., 2019; Hong et al., 2022). In our case, the upper level problem (PDE inverse problem) is usually non-convex, and the lower level problem has a challenging loss landscape (Krishnapriyan et al., 2021; Basir & Senocak, 2022a). However, the lower level problem does not need to be solved to optimality at each iteration because the primary goal is to approximate the descent direction for the upper level problem. We propose to apply gradient descent to the upper and lower level optimization problems simultaneously. In Algorithm. 1, we describe our optimization algorithm for inferring scalar parameters in the BiLO framework. The algorithm for inferring unknown functions is similar. We write the algorithm as simple gradient descent for notational simplicity, while in practice we use ADAM (Kingma & Ba, 2017).

We are able to obtain a theoretical characterization of the bilevel optimization problem:

Theorem 2.1. *Assuming (i) the maximum principal holds for the PDE operator; (ii) the parametrized local operator $u(W, \Theta) = g$ on $\partial\Omega$ for all W and Θ ; (iii) the*

Algorithm 1 Bi-level Local Operator for inferring scalar PDE parameters

- 1: **Input:** Collections of collocation points \mathcal{T}_{res} and \mathcal{T}_{dat} , initial guess of the PDE parameters Θ_0
- 2: **Pre-train:** Solve the lower level problem at fixed Θ_0 :

$$\min_W \mathcal{L}_{\text{LO}}(\Theta_0, W)$$

- 3: **Fine-Tune:** Simultaneous gradient descent at the upper and lower level (7).

$$\begin{cases} \Theta^{k+1} = \Theta^k - lr_{\Theta} \nabla_{\Theta} \mathcal{L}_{\text{dat}}(\Theta^k, W^k) & (9) \\ W^{k+1} = W^k - lr_W \nabla_W \mathcal{L}_{\text{LO}}(\Theta^k, W^k) & (10) \end{cases}$$

lower level problem has a minimizer $W^(\Theta)$ such that the $u(W^*(\Theta), \Theta)$ is the local operator, then the approximate gradient of the upper level objective at $W^*(\Theta)$ is exact.*

The proof is shown in Appendix C, where we analyze the hypergradient of the upper level problem and the approximate gradient during the Simultaneous Gradient Descent process. In our numerical examples, we show that our method can applied under much less restrictive conditions. In addition, it is not imperative for the residual-gradient loss to be minimized excessively; it is sufficient that it approximate the correct descent direction. We can have two different learning rates for the two groups of variables W and Θ , denoted as lr_W and lr_{Θ} , respectively. We empirically determined $w_{\text{rgrad}} = 0.001$ and $lr_W = lr_{\Theta} = 0.001$ to be effective across our numerical experiments.

2.4. Difference between BiLO, PINN, and NO

Neural Operator (NO) Neural operators can serve as surrogate models for PDE solution operators, and can be used in algorithms that require solving the forward PDE multiple times, such as Bayesian inference or derivative-free optimization (Kaltenbach et al., 2023; Lu et al., 2022b), or gradient-based optimization algorithms (Zhou et al., 2024; Lu et al., 2022b; Yang et al., 2023b). However, if the objective is to estimate parameters from limited data, the considerable initial cost for data generation and network training might seem excessive. The accuracy of specific PDE solutions depends on the accuracy of the neural operator, and which may decrease if the true PDE parameters fall outside the training data’s distribution (de Hoop et al., 2022). Thus, in the context of finding the best estimate of the parameters given the data in a PDE-constrained optimization framework, we mainly compare BiLO with PINNs.

PINN Within the PINN framework, the solution of the PDE is represented by a deep neural network $u(\mathbf{x}; W)$, where W denotes all the trainable weights of the neural network

(Karniadakis et al., 2021; Raissi et al., 2019; Lu et al., 2021b). Notice that the PDE parameters Θ are not part of the network input. Therefore the data loss does not depend on the PDE parameters Θ directly, and we write the data loss as $\mathcal{L}_{\text{dat}}(W)$.

Solving an inverse problem using PINN involves minimizing an unconstrained optimization problem, where the objective function is the weighted sum of the residual loss and the data loss

$$\min_{W, \Theta} \mathcal{L}_{\text{res}}(W, \Theta) + w_{\text{dat}} \mathcal{L}_{\text{dat}}(W) \quad (11)$$

where w_{dat} is the weight of the data loss. The key feature is that the PDE is enforced as a soft constraint, or as a regularization term for fitting the data. The relationship between the PDE parameter and the data loss is indirect: the descent directions of the PDE parameters are given by $\nabla_{\Theta} \mathcal{L}_{\text{res}}$, which does not directly depend on the data loss.

Challenges for PINNs Solving PDE inverse problems using PINNs can encounter challenges stemming from the soft PDE constraint (11), especially when the data is sparse and noisy, or when the PDE model does not fully explain the data (Zhang et al., 2024a). The soft PDE constraint can result in a trade-off between fitting the data and solving the PDE accurately. In addition, since the PDE parameters are updated in the descent direction of the residual loss, they can be biased toward parameters corresponding to very smooth solutions. It is important to recognize that PINNs can indeed be effective for PDE inverse problems, if the weights are chosen properly.

There are many techniques to improve the performance of PINNs, such as adaptive sampling and weighting of collocation points (Nabian et al., 2021; Wu et al., 2023; Lu et al., 2021b; Anagnostopoulos et al., 2024), new architectures (Jagtap & Karniadakis, 2020; Wang et al., 2024; 2021a; Moseley et al., 2023), new optimization algorithms (Basir & Senocak, 2022b; Krishnapriyan et al., 2021), new loss functions (Wang et al., 2022; Yu et al., 2022; Son et al., 2021), adaptive weighting of loss terms (Maddu et al., 2022; Wang et al., 2021a; McClenny & Braga-Neto, 2022; Wang et al., 2023). However, these techniques do not fundamentally change the soft PDE-constraints in the PINN framework. In our work, we propose a different optimization problem that does not involve a trade-off between the residual loss and the data loss, and our method can be used in conjunction with many of these techniques to improve the performance. Therefore, in the following numerical experiments, we do not use any of these techniques, and we focus on comparing the two different optimization formulations (BiLO and the soft PDE-constraints).

The challenge of balancing trade-offs also motivated the Bilevel PINN (BPN) (Hao et al., 2023), which applies a bilevel optimization framework to PDE inverse problems

by representing the PDE solution with a neural network, using the residual loss for the lower-level problem, and approximating the upper-level hypergradient with Broyden’s method. In contrast, our approach incorporates the PDE parameter as part of the network input, with the lower-level problem focused on approximating the local operator, allowing more direct computation of the upper-level descent direction. We compare BPN and BiLO in Appendix F.

3. Numerical Experiments

We evaluate the effectiveness of our method on a diverse set of PDE inverse problems, encompassing elliptic, parabolic, and hyperbolic systems. Our test cases include challenging scenarios such as nonlinear dynamics, singular forcing terms, real-world data applications, and objective functions that extend beyond simple mean squared error (MSE). In our experiments, we denote the neural network solution (obtained via BiLO, PINN, or NO) as u_{NN} , and the numerical solution computed with the inferred parameters using the Finite Difference Method (FDM) as u_{FDM} , which is computed to high accuracy and serves as the exact solution to measure the accuracy of the neural network solution. We consider Gaussian noise with mean 0 and standard deviation σ . The training details for the numerical experiments in Appendix D. The computational costs are provided in Appendix E.

3.1. Fisher-KPP Equation

We aim to infer the unknown parameters D and ρ in the following nonlinear reaction-diffusion equation (Fisher-KPP equation) as in Zou et al. (2024):

$$\begin{cases} u_t(x, t) = 0.01 D u_{xx}(x, t) + \rho u(1 - u) \\ u(x, 0) = \frac{1}{2} \sin(\pi x)^2, \quad u(0, t) = u(1, t) = 0. \end{cases}$$

The initial guesses of the PDE parameters are $D_0 = 1$ and $\rho_0 = 1$, and the ground truth parameters are $D_{GT} = 2$ and $\rho_{GT} = 2$. This equation has been used to model various biological phenomena, such as the growth of tumors (Swanson et al., 2000; Harpold et al., 2007) or the spreading of misfolded proteins (Schäfer et al., 2020; 2021; Zhang et al., 2024b).

Sparse and Noisy Data The data is only provided at 9 points at the final time $t = 1$, which resides on a lower dimensional manifold of the solution surface, while we are still interested in solving the PDE from $t = 0$ to $t = 1$ accurately. This single-time inference problem has application in patient-specific parameter estimation of tumor growth models using medical images, where only one time point may be available, e.g., in the case of glioblastoma (Balcerak et al., 2024; Zhang et al., 2024a; Ezhov et al., 2023; Scheufele et al., 2021).

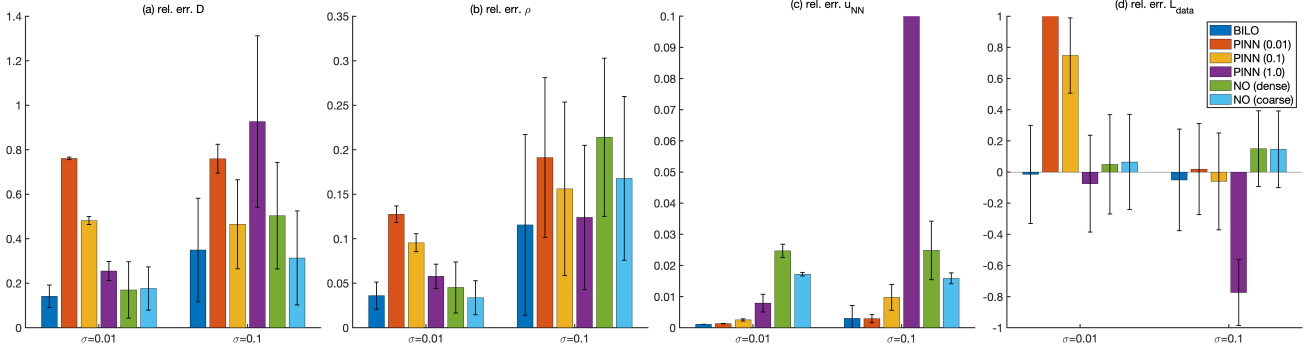


Figure 2: Comparison of performance metrics for varying $\sigma = 10^{-2}, 10^{-1}$ across different methods: BiLO, PINN (with $w_{\text{dat}} = 0.01, 0.1, 1$), and NO (with different pretrain datasets).

Results We solve the inverse problem using different methods under varying noise levels ($\sigma = 10^{-2}, 10^{-1}$) across five random seeds. Due to the presence of noise, the global minimum is unknown. However, the mean of the inferred parameters, D and ρ , across different noise realizations should be close to the ground truth values. Additionally, for the ground truth solution, the average data loss should equal the noise variance. To assess this, we compute the relative error of the data loss, defined as $(\mathcal{L}_{\text{dat}} - \sigma^2)/\sigma^2$, where a positive value indicates underfitting and a negative value suggests overfitting.

Figure 2 presents the mean and standard deviation (std) of various metrics: (a) and (b) show the relative error of the inferred parameters D and ρ with respect to the ground truth, (c) depicts the relative L2 error of u_{NN} compared to u_{FDM} , and (d) illustrates the relative error of the data loss. We evaluate three approaches: (1) BiLO, (2) PINNs with different w_{dat} , and (3) Neural Operator (NO) with varying pretraining datasets. For NO, we pretrain DeepONets on numerical PDE solutions corresponding to different values of D and ρ , considering both coarse and dense parameter sampling. A gradient-based optimization algorithm is then used to solve the inverse problem.

Several key observations emerge from Fig. 2: (1) BiLO achieves the best performance in terms of parameter inference for D and ρ , as well as PDE solution accuracy, without exhibiting overfitting or underfitting tendencies. (2) The performance of PINNs is highly sensitive to the choice of w_{dat} , with the optimal value depending on the noise level. A relatively large w_{dat} reduces PDE solution accuracy and tends to cause overfitting. (3) The performance of NO depends on the pretraining dataset, with lower accuracy than PINN/BiLO but more stable across different noise levels.

3.2. Elliptic Equation with Singular Forcing

We consider the following elliptic equation with singular forcing, which describe gene expression of a 1D cell (Miles

et al., 2024)

$$\Delta u + \lambda \delta(x - z) - \mu u = 0, \quad u(0) = u(1) = 0,$$

where $z = 0.5$ is the gene site, μ is the switch rate, λ is the birth rate, and $u(x)$ is the intensity measure of the Poisson spatial process, which is related to probability of observing a particle (mRNA) at location x .

Given M snapshot of particle locations q_i^j for $i = 1, \dots, N_j$ and $j = 1, \dots, M$, we aim to infer the parameters λ and μ , by minimizing the negative log-likelihood function:

$$\min_{\lambda, \mu} M \int u(x) dx - \sum_{j=1}^M \sum_{i=1}^{N_j} \log u(q_i^j)$$

The solution of the PDE is continuous but the derivative is discontinuous at z . We handle the singular forcing using the cusp-capturing PINN (Tseng et al., 2023). The objective function is also more challenging than the MSE, as the values of u is not available at the particle locations. The particle positions are sampled using ground truth parameters $\lambda_{\text{GT}} = 250$ and $\mu_{\text{GT}} = 5$ with $M = 100$. We take initial guess $\lambda_0 = 500$ and $\mu_0 = 2.5$. Additional details are provided in Appendix D.2. The results are shown in Fig. 3, and BiLO achieve significantly better performance than PINN (cross validated with various w_{dat}).

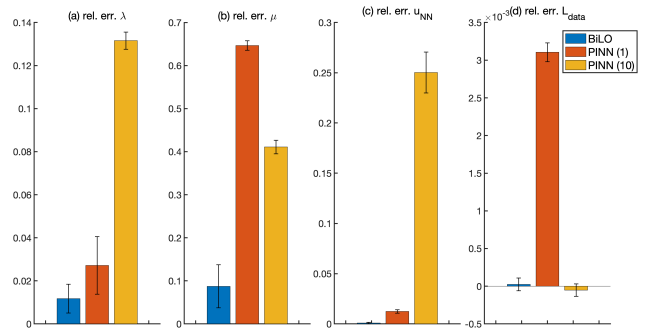


Figure 3: Comparison of performance metrics for BiLO and PINN ($w_{\text{dat}} = 1$ and 10) for the elliptic equation with singular forcing.

3.3. Poisson Equation with Variable Diffusion

We consider the following Poisson equation

$$-(D(x)u'(x))' = f(x), u(0) = u(1) = 0, x \in [0, 1],$$

where $f(x) = \pi^2 \sin(\pi x)$. We aim to infer the variable diffusion coefficient $D(x)$ such that $D(0) = D(1) = 1$. The ground truth $D(x)$ is a ‘‘hat’’ function $D(x) = 1 + 0.5x$ for $x \in [0, 0.5]$ and $D(x) = 1.5 - 0.5x$ for $x \in [0.5, 1]$ and the initial guess is $D_0(x) = 1$.

Results We perform inference under noise $\sigma = 0.01$ with $w_{\text{reg}} = 10^{-3}$. Figure 4 presents the mean and standard deviation of various metrics across five random seeds: (a) the relative L_2 error of the inferred function $D(x)$ compared to the ground truth D_{GT} , (b) the relative L_2 error between u_{NN} and u_{FDM} , and (c) the relative error of the data loss, $(\mathcal{L}_{\text{dat}} - \sigma^2)/\sigma^2$, which indicates tendencies for overfitting or underfitting.

We evaluate BiLO, PINNs with $w_{\text{dat}} = 1, 10, 100$, the adjoint method, and NO with different pretraining datasets (Gaussian random fields with varying correlation lengths). Overall, BiLO achieves the best performance across all metrics. The performance of PINN is sensitive to w_{dat} , where a large w_{dat} leads to overfitting, while a small w_{dat} results in underfitting. The accuracy of NO depends on the choice of the pretraining dataset. The adjoint method, which solves the PDE with high accuracy and is considered ‘‘exact’’ (hence no corresponding bar in (b)), reconstructs the diffusion coefficient less accurately than BiLO. Further details are provided in Appendix D.3.

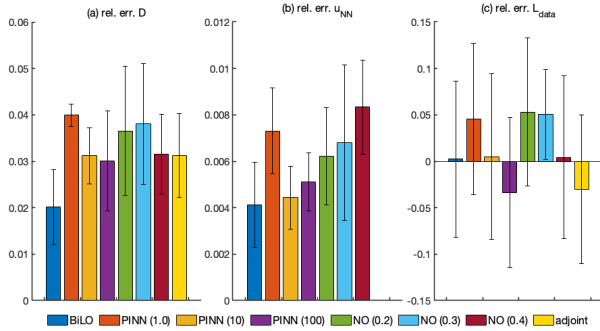


Figure 4: Comparison of performance metrics for different methods: BiLO, PINN (with various w_{dat}), the adjoint method, and NO (with different Gaussian random fields length scale as training dataset).

3.4. Inviscid Burger’s Equation

We consider an inverse problem governed by an inviscid Burger’s equation on the domain $x \in [0, 1]$ and $t \in [0, 1]$.

$$u_t + auu_x = 0, u(x, 0) = f(x), u(0, t) = u(1, t) = 0$$

where $a = 0.2$. We aim to infer the initial condition f from the observational data at $t = 1$. The numerical solutions are computed by using the Godunov scheme. The inviscid Burger’s equation is a hyperbolic PDE, and the solution can develop shocks and rarefaction waves.

Fig. 5 shows one example of inferring the initial condition of the Burger’s equation. We show the initial guess in the first column, the ground truth in the second column, and the inference results by BiLO in the third column. The first row shows the initial condition $f(x)$, the second rows shows the solution $u(x, t)$ on the domain $x \in [0, 1]$ and $t \in [0, 1]$, and the third row shows the solution $u(x, 1)$. Notice that for inference, only solution at $t = 1$ of the ground truth is provided. We can see that the BiLO can accurately infer the initial condition of the Burger’s equation, even when the solution is non-smooth. Additional examples are shown in Appendix D.5.

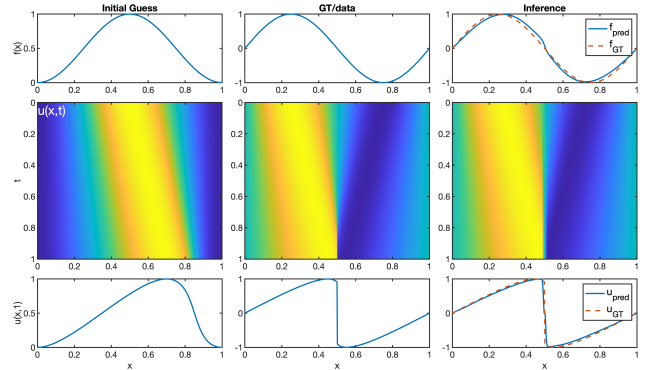


Figure 5: Example of inferring the initial condition of the inviscid Burger’s equation using data at $t = 1$.

In Appendix D.4, we also show detailed results of inferring the initial condition of the heat equation, which is a parabolic PDE and is a classical example of ill-posed inverse problem.

3.5. Darcy Flow in 2D

The setup of this experiment is similar to the steady state Darcy flow inverse problem in Li et al. (2024). We consider the following 2D Poisson equation with variable diffusion coefficient in the unit square domain $\Omega = [0, 1] \times [0, 1]$ with Dirichlet boundary condition:

$$\begin{cases} -\nabla \cdot (A(\mathbf{x})\nabla u(\mathbf{x})) = f(\mathbf{x}) & \text{in } \Omega \\ u(\mathbf{x}) = 0, & \text{on } \partial\Omega \end{cases}$$

Our goal is to infer the variable diffusion coefficient $A(\mathbf{x})$ from the solution $u(\mathbf{x})$. Figure 6 shows an example of our experiment. the relative error of the inferred diffusion coefficient is 1.3% and the thresholded the inferred diffusion coefficient (dashed line) has the classification accuracy is 98%, which is comparable to the results (2.29%

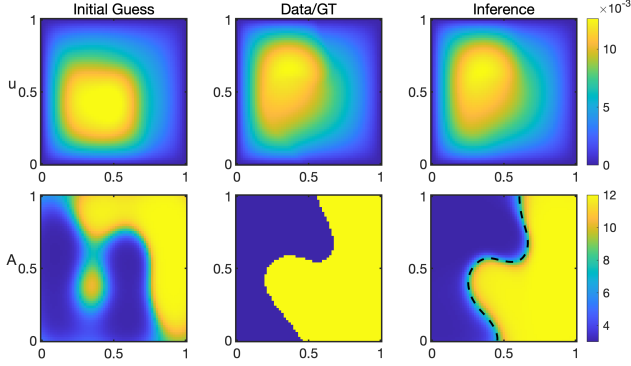


Figure 6: Example of Darcy Inverse problem

relative 12 error on u and 97.10% classification accuracy) from the Physics-informed Neural Operator (PINO) in Li et al. (2024), which require pretraining a FNO with synthetic dataset, and instance-wise fine-tuning with physics-informed loss. For our method, we only need to pretrain the BiLO with a single initial guess, which can be very different from the ground truth. Additional examples are shown in Appendix D.6.

3.6. Glioblastoma (GBM) Inverse Problem

In this section, we consider a real-world application of BiLO for patient specific parameter estimation of GBM growth models using patient MRI data in 2D. The challenge lies in the high noise levels and the potential model misspecification, as the Fisher-KPP PDE may not fully capture the complexities present in the tumor MRI data. The setup of the problem follows Zhang et al. (2024a); Balcerak et al. (2024); Ezhov et al. (2023); Scheufele et al. (2021).

Tumor Growth and Imaging Model Let Ω be the brain region in 2D based on MRI images. The normalized tumor cell density is $u(\mathbf{x}, t)$.

$$\begin{cases} \frac{\partial u}{\partial t} = D\bar{D}\nabla \cdot (P(\mathbf{x})\nabla u) + \rho\bar{\rho}u(1-u) & \text{in } \Omega \\ \nabla u \cdot \mathbf{n} = 0 & \text{on } \partial\Omega \end{cases}$$

where P depends on the tissue distribution, and \bar{D} , $\bar{\rho}$ are known patient specific characteristic parameters based on the data. D and ρ are the unknown nondimensionalized parameters that we aim to infer from the data. Let \mathbf{y}^s , $s \in \{\text{WT}, \text{TC}\}$ be indicator function of the whole tumor (WT) region and tumor core (TC) region, respectively. We assume that the segmentations are tumor cell density u at nondimensional $t = 1$ above certain thresholds u_c^s . The predicted segmentations \mathbf{y}_{pred}^s are given by applying a smooth thresholding function to the tumor cell density u at $t = 1$. We aim to minimize the relative error between the predicted segmentations and segmentation data:

$$\min_{D, \rho, u_c^{\text{WT}}, u_c^{\text{TC}}} \sum_{s \in \{\text{WT}, \text{TC}\}} \|\mathbf{y}_{pred}^s - \mathbf{y}^s\|_2^2 / \|\mathbf{y}^s\|_2^2$$

Results In this numerical experiment, no ground truth is available for the parameters D , ρ , u_c^{WT} , and u_c^{TC} . We quantify the performance of the inferred parameters by the DICE score between the predicted segmentations and the segmentation data. Table 1 shows the relative error of the u_{NN} and u_{FDM} at $t = 1$ and $\text{DICE}_{\text{m}}^{\text{WT}}$, which denotes the DICE scores between the data segmentation and the predicted segmentation of the WT region based on u_{FDM} or u_{NN} . Fig 7 shows the predicted segmentations using BiLO and PINN with different w_{dat} . For PINN, the DICE score based on u_{NN} is generally higher than that of u_{FDM} , indicating a tendency to overfit the data at the expense of the accuracy of the PDE solution, which is also reflected in the large relative error of u_{NN} . This overfitting is also evident in Fig 7, where the contours of the predicted segmentations based on u_{NN} tends to follow the noisy segmentation data more closely than the FDM solution. Reducing w_{dat} helps mitigate this discrepancy. Despite this, the inferred parameters can still have good performance, as shown by the DICE score based on u_{FDM} . Overall, BiLO provides an accurate PDE solution and well-performing parameters without the need to tune the data weight, and leads to slightly better parameters in this case.

Table 1: Results of the GBM inverse problem: DICE score of predicted segmentations based on u_{NN} and u_{FDM} and the relative MSE of u_{NN}

methods	$\text{DICE}_{\text{NN}}^{\text{WT}}$	$\text{DICE}_{\text{FDM}}^{\text{WT}}$	rel.MSE(%)
PINN(1e-3)	0.88	0.80	9.5
PINN(1e-5)	0.81	0.80	0.5
BiLO	0.81	0.81	0.3

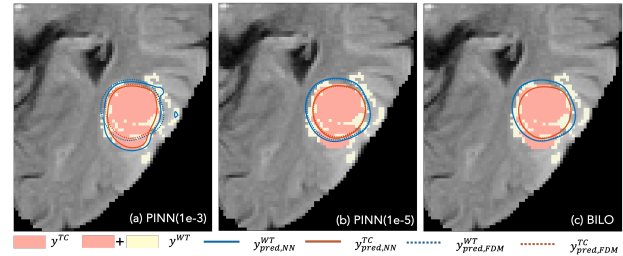


Figure 7: Predicted segmentation using PINN with $w_{\text{dat}} = 10^{-3}$, 10^{-5} and BiLO. The solid and dashed contours are the predicted segmentation based on u_{NN} and u_{FDM} . BiLO gives almost overlapping contours, suggesting high accuracy of u_{NN} .

4. Conclusion

In this work, we propose a Bi-level Local Operator (BiLO) learning framework for solving PDE inverse problems: we minimize the data loss with respect to the PDE parameters at the upper level, and learn the local solution oper-

ator of the PDE at the lower level. The bi-level optimization problem is solved using simultaneous gradient descent, leading to an efficient algorithm. Empirical results demonstrate more accurate parameter recovery and stronger fidelity to the underlying PDEs under sparse and noisy data, compared with the soft PDE-constraint formulation, which faces the delicate trade-off between adhering to the PDE constraints and accurately fitting the data.

Code Availability

The code for the numerical experiments is available at <https://github.com/Rayzhangzirui/BiLO>.

Acknowledgment

R.Z.Z and J.S.L thank Babak Shahbaba for the GPU resources. R.Z.Z thank Christopher E. Miles for the helpful discussion on the example of inferring stochastic rates from particle positions. J.S.L acknowledges partial support from the National Science Foundation through grants DMS-2309800, DMS-1953410 and DMS-1763272 and the Simons Foundation (594598QN) for an NSF-Simons Center for Multiscale Cell Fate Research.

References

- Anagnostopoulos, S. J., Toscano, J. D., Stergiopoulos, N., and Karniadakis, G. E. Residual-based attention in physics-informed neural networks. *Computer Methods in Applied Mechanics and Engineering*, 421:116805, March 2024. ISSN 0045-7825. doi: 10.1016/j.cma.2024.116805.
- Balcerak, M., Weidner, J., Karnakov, P., Ezhov, I., Litvinov, S., Koumoutsakos, P., Zhang, R. Z., Lowengrub, J. S., Wiestler, B., and Menze, B. Individualizing Glioma Radiotherapy Planning by Optimization of Data and Physics-Informed Discrete Loss, February 2024.
- Basir, S. and Senocak, I. Critical Investigation of Failure Modes in Physics-informed Neural Networks, June 2022a.
- Basir, S. and Senocak, I. Physics and equality constrained artificial neural networks: Application to forward and inverse problems with multi-fidelity data fusion. *Journal of Computational Physics*, 463:111301, August 2022b. ISSN 0021-9991. doi: 10.1016/j.jcp.2022.111301.
- Broyden, C. G. A class of methods for solving nonlinear simultaneous equations. *Mathematics of Computation*, 19(92):577–593, 1965. ISSN 0025-5718, 1088-6842. doi: 10.1090/S0025-5718-1965-0198670-6.
- Brunton, S. L. and Kutz, J. N. Machine Learning for Partial Differential Equations, March 2023.
- Chen, Y., Lu, L., Karniadakis, G. E., and Negro, L. D. Physics-informed neural networks for inverse problems in nano-optics and metamaterials. *Optics Express*, 28(8):11618–11633, April 2020. ISSN 1094-4087. doi: 10.1364/OE.384875.
- Constantine, P. Random Field Simulation. MATLAB Central File Exchange, 2024.

- de Hoop, M. V., Huang, D. Z., Qian, E., and Stuart, A. M. The Cost-Accuracy Trade-Off In Operator Learning With Neural Networks, August 2022.
- Deng, C., Feng, S., Wang, H., Zhang, X., Jin, P., Feng, Y., Zeng, Q., Chen, Y., and Lin, Y. OpenFWI: Large-Scale Multi-Structural Benchmark Datasets for Seismic Full Waveform Inversion, June 2023.
- Dong, S. and Ni, N. A method for representing periodic functions and enforcing exactly periodic boundary conditions with deep neural networks. *Journal of Computational Physics*, 435:110242, June 2021. ISSN 0021-9991. doi: 10.1016/j.jcp.2021.110242.
- Evans, L. C. *Partial Differential Equations*. American Mathematical Soc., 2010. ISBN 978-0-8218-4974-3.
- Ezhov, I., Scibilia, K., Franitza, K., Steinbauer, F., Shit, S., Zimmer, L., Lipkova, J., Kofler, F., Paetzold, J. C., Canalini, L., Waldmannstetter, D., Menten, M. J., Metz, M., Wiestler, B., and Menze, B. Learn-Morph-Infer: A new way of solving the inverse problem for brain tumor modeling. *Medical Image Analysis*, 83:102672, January 2023. ISSN 1361-8415. doi: 10.1016/j.media.2022.102672.
- Hao, Z., Ying, C., Su, H., Zhu, J., Song, J., and Cheng, Z. Bi-level Physics-Informed Neural Networks for PDE Constrained Optimization using Broyden’s Hypergradients, April 2023.
- Harpold, H., Alvord Jr., E., and Swanson, K. The evolution of mathematical modeling of glioma proliferation and invasion. *Journal of Neuropathology and Experimental Neurology*, 66(1):1–9, 2007. doi: 10.1097/nen.0b013e31802d9000.
- Herrmann, L. and Kollmannsberger, S. Deep learning in computational mechanics: A review. *Computational Mechanics*, January 2024. ISSN 1432-0924. doi: 10.1007/s00466-023-02434-4.
- Hinze, M., Pinnau, R., Ulbrich, M., and Ulbrich, S. *Optimization with PDE Constraints*. Springer Science & Business Media, October 2008. ISBN 978-1-4020-8839-1.
- Hong, M., Wai, H.-T., Wang, Z., and Yang, Z. A Two-Timescale Framework for Bilevel Optimization: Complexity Analysis and Application to Actor-Critic, June 2022.
- Jagtap, A. D. and Karniadakis, G. E. Adaptive activation functions accelerate convergence in deep and physics-informed neural networks. *Journal of Computational Physics*, 404:109136, March 2020. ISSN 00219991. doi: 10.1016/j.jcp.2019.109136.
- Jagtap, A. D., Mao, Z., Adams, N., and Karniadakis, G. E. Physics-informed neural networks for inverse problems in supersonic flows. *Journal of Computational Physics*, 466:111402, October 2022a. ISSN 0021-9991. doi: 10.1016/j.jcp.2022.111402.
- Jagtap, A. D., Mitsotakis, D., and Karniadakis, G. E. Deep learning of inverse water waves problems using multi-fidelity data: Application to Serre–Green–Naghdi equations. *Ocean Engineering*, 248:110775, March 2022b. ISSN 0029-8018. doi: 10.1016/j.oceaneng.2022.110775.
- Kaltenbach, S., Perdikaris, P., and Koutsourelakis, P.-S. Semi-supervised Invertible Neural Operators for Bayesian Inverse Problems, March 2023.
- Kapoor, T., Wang, H., Nunez, A., and Dollevoet, R. Physics-informed neural networks for solving forward and inverse problems in complex beam systems. *IEEE Transactions on Neural Networks and Learning Systems*, pp. 1–15, 2024. ISSN 2162-237X, 2162-2388. doi: 10.1109/TNNLS.2023.3310585.
- Karnakov, P., Litvinov, S., and Koumoutsakos, P. Optimizing a Discrete Loss (ODIL) to solve forward and inverse problems for partial differential equations using machine learning tools, May 2022.
- Karniadakis, G. E., Kevrekidis, I. G., Lu, L., Perdikaris, P., Wang, S., and Yang, L. Physics-informed machine learning. *Nature Reviews Physics*, 3(6):422–440, June 2021. ISSN 2522-5820. doi: 10.1038/s42254-021-00314-5.
- Khanduri, P., Tsaknakis, I., Zhang, Y., Liu, J., Liu, S., Zhang, J., and Hong, M. Linearly Constrained Bilevel Optimization: A Smoothed Implicit Gradient Approach. In *Proceedings of the 40th International Conference on Machine Learning*, pp. 16291–16325. PMLR, July 2023.
- Kingma, D. P. and Ba, J. Adam: A Method for Stochastic Optimization, January 2017.
- Kovachki, N., Li, Z., Liu, B., Azizzadenesheli, K., Bhattacharya, K., Stuart, A., and Anandkumar, A. Neural Operator: Learning Maps Between Function Spaces, October 2022.
- Krishnapriyan, A. S., Gholami, A., Zhe, S., Kirby, R. M., and Mahoney, M. W. Characterizing possible failure modes in physics-informed neural networks, November 2021.
- Li, Z., Kovachki, N., Azizzadenesheli, K., Liu, B., Bhattacharya, K., Stuart, A., and Anandkumar, A. Fourier Neural Operator for Parametric Partial Differential Equations, May 2021.

- Li, Z., Zheng, H., Kovachki, N., Jin, D., Chen, H., Liu, B., Azizzadenesheli, K., and Anandkumar, A. Physics-Informed Neural Operator for Learning Partial Differential Equations. *ACM / IMS Journal of Data Science*, 1(3):9:1–9:27, May 2024. doi: 10.1145/3648506.
- Lipková, J., Angelikopoulos, P., Wu, S., Alberts, E., Wiestler, B., Diehl, C., Preibisch, C., Pyka, T., Combs, S. E., Hadjidoukas, P., Van Leemput, K., Koumoutsakos, P., Lowengrub, J., and Menze, B. Personalized Radiotherapy Design for Glioblastoma: Integrating Mathematical Tumor Models, Multimodal Scans, and Bayesian Inference. *IEEE Transactions on Medical Imaging*, 38(8):1875–1884, August 2019. ISSN 1558-254X. doi: 10.1109/TMI.2019.2902044.
- Lu, L., Jin, P., Pang, G., Zhang, Z., and Karniadakis, G. E. Learning nonlinear operators via DeepONet based on the universal approximation theorem of operators. *Nature Machine Intelligence*, 3(3):218–229, March 2021a. ISSN 2522-5839. doi: 10.1038/s42256-021-00302-5.
- Lu, L., Meng, X., Mao, Z., and Karniadakis, G. E. DeepXDE: A Deep Learning Library for Solving Differential Equations. *SIAM Review*, 63(1):208–228, January 2021b. ISSN 0036-1445, 1095-7200. doi: 10.1137/19M1274067.
- Lu, L., Pestourie, R., Yao, W., Wang, Z., Verdugo, F., and Johnson, S. G. Physics-Informed Neural Networks with Hard Constraints for Inverse Design. *SIAM Journal on Scientific Computing*, 43(6):B1105–B1132, January 2021c. ISSN 1064-8275. doi: 10.1137/21M1397908.
- Lu, L., Meng, X., Cai, S., Mao, Z., Goswami, S., Zhang, Z., and Karniadakis, G. E. A comprehensive and fair comparison of two neural operators (with practical extensions) based on FAIR data. *Computer Methods in Applied Mechanics and Engineering*, 393:114778, April 2022a. ISSN 0045-7825. doi: 10.1016/j.cma.2022.114778.
- Lu, L., Pestourie, R., Johnson, S. G., and Romano, G. Multifidelity deep neural operators for efficient learning of partial differential equations with application to fast inverse design of nanoscale heat transport. *Physical Review Research*, 4(2):023210, June 2022b. doi: 10.1103/PhysRevResearch.4.023210.
- Maddu, S., Sturm, D., Müller, C. L., and Sbalzarini, I. F. Inverse Dirichlet weighting enables reliable training of physics informed neural networks. *Machine Learning: Science and Technology*, 3(1):015026, February 2022. ISSN 2632-2153. doi: 10.1088/2632-2153/ac3712.
- Mao, S., Dong, R., Lu, L., Yi, K. M., Wang, S., and Perdikaris, P. PPDONet: Deep Operator Networks for Fast Prediction of Steady-state Solutions in Disk–Planet Systems. *The Astrophysical Journal Letters*, 950(2):L12, June 2023. ISSN 2041-8205. doi: 10.3847/2041-8213/acd77f.
- Martin, J., Wilcox, L. C., Burstedde, C., and Ghattas, O. A Stochastic Newton MCMC Method for Large-Scale Statistical Inverse Problems with Application to Seismic Inversion. *SIAM Journal on Scientific Computing*, 34(3):A1460–A1487, January 2012. ISSN 1064-8275, 1095-7197. doi: 10.1137/110845598.
- McClenney, L. and Braga-Neto, U. Self-Adaptive Physics-Informed Neural Networks using a Soft Attention Mechanism, April 2022.
- Miles, C. E., McKinley, S. A., Ding, F., and Lehoucq, R. B. Inferring Stochastic Rates from Heterogeneous Snapshots of Particle Positions. *Bulletin of Mathematical Biology*, 86(6):74, May 2024. ISSN 1522-9602. doi: 10.1007/s11538-024-01301-4.
- Molinaro, R., Yang, Y., Engquist, B., and Mishra, S. Neural Inverse Operators for Solving PDE Inverse Problems, June 2023.
- Moseley, B., Markham, A., and Nissen-Meyer, T. Finite basis physics-informed neural networks (FBPINNs): A scalable domain decomposition approach for solving differential equations. *Advances in Computational Mathematics*, 49(4):62, July 2023. ISSN 1572-9044. doi: 10.1007/s10444-023-10065-9.
- Nabian, M. A., Gladstone, R. J., and Meidani, H. Efficient training of physics-informed neural networks via importance sampling. *Computer-Aided Civil and Infrastructure Engineering*, 36(8):962–977, 2021. ISSN 1467-8667. doi: 10.1111/mice.12685.
- Nganyu Tanyu, D., Ning, J., Freudenberg, T., Heilenkötter, N., Rademacher, A., Iben, U., and Maass, P. Deep learning methods for partial differential equations and related parameter identification problems. *Inverse Problems*, 39(10):103001, October 2023. ISSN 0266-5611, 1361-6420. doi: 10.1088/1361-6420/ace9d4.
- O’Leary-Roseberry, T., Chen, P., Villa, U., and Ghattas, O. Derivative-Informed Neural Operator: An efficient framework for high-dimensional parametric derivative learning. *Journal of Computational Physics*, 496:112555, January 2024. ISSN 0021-9991. doi: 10.1016/j.jcp.2023.112555.
- Pathak, J., Subramanian, S., Harrington, P., Raja, S., Chattopadhyay, A., Mardani, M., Kurth, T., Hall, D., Li, Z., Azizzadenesheli, K., Hassanzadeh, P., Kashinath, K.,

- and Anandkumar, A. FourCastNet: A Global Data-driven High-resolution Weather Model using Adaptive Fourier Neural Operators, February 2022.
- Pedregosa, F. Hyperparameter optimization with approximate gradient, November 2022.
- Plessix, R.-E. A review of the adjoint-state method for computing the gradient of a functional with geophysical applications. *Geophysical Journal International*, 167(2):495–503, November 2006. ISSN 0956-540X. doi: 10.1111/j.1365-246X.2006.02978.x.
- Raissi, M., Perdikaris, P., and Karniadakis, G. E. Physics-informed neural networks: A deep learning framework for solving forward and inverse problems involving nonlinear partial differential equations. *Journal of Computational Physics*, 378:686–707, February 2019. ISSN 0021-9991. doi: 10.1016/j.jcp.2018.10.045.
- Schäfer, A., Mormino, E. C., and Kuhl, E. Network Diffusion Modeling Explains Longitudinal Tau PET Data. *Frontiers in Neuroscience*, 14, 2020. ISSN 1662-453X.
- Schäfer, A., Peirlinck, M., Linka, K., and Kuhl, E. Bayesian Physics-Based Modeling of Tau Propagation in Alzheimer’s Disease. *Frontiers in Physiology*, 12:702975, July 2021. ISSN 1664-042X. doi: 10.3389/fphys.2021.702975.
- Scheufele, K., Subramanian, S., and Biros, G. Fully Automatic Calibration of Tumor-Growth Models Using a Single mpMRI Scan. *IEEE Transactions on Medical Imaging*, 40(1):193–204, January 2021. ISSN 1558-254X. doi: 10.1109/TMI.2020.3024264.
- Sen, M. K. and Stoffa, P. L. *Global Optimization Methods in Geophysical Inversion*. Cambridge University Press, Cambridge, 2013. ISBN 978-1-107-01190-8. doi: 10.1017/CBO9780511997570.
- Shaban, A., Cheng, C.-A., Hatch, N., and Boots, B. Truncated Back-propagation for Bilevel Optimization. In *Proceedings of the Twenty-Second International Conference on Artificial Intelligence and Statistics*, pp. 1723–1732. PMLR, April 2019.
- Shen, H., Xiao, Q., and Chen, T. On Penalty-based Bilevel Gradient Descent Method, September 2023.
- Son, H., Jang, J. W., Han, W. J., and Hwang, H. J. Sobolev Training for Physics Informed Neural Networks, December 2021.
- Stuart, A. M. Inverse problems: A Bayesian perspective. *Acta Numerica*, 19:451–559, May 2010. ISSN 1474-0508, 0962-4929. doi: 10.1017/S0962492910000061.
- Subramanian, S., Ghafouri, A., Scheufele, K. M., Himthani, N., Davatzikos, C., and Biros, G. Ensemble Inversion for Brain Tumor Growth Models With Mass Effect. *IEEE Transactions on Medical Imaging*, 42(4):982–995, April 2023. ISSN 1558-254X. doi: 10.1109/TMI.2022.3221913.
- Sukumar, N. and Srivastava, A. Exact imposition of boundary conditions with distance functions in physics-informed deep neural networks. *Computer Methods in Applied Mechanics and Engineering*, 389:114333, February 2022. ISSN 0045-7825. doi: 10.1016/j.cma.2021.114333.
- Swanson, K., Alvord E.C., Jr., and Murray, J. A quantitative model for differential motility of gliomas in grey and white matter. *Cell Proliferation*, 33(5):317–329, 2000. doi: 10.1046/j.1365-2184.2000.00177.x.
- Tseng, Y.-H., Lin, T.-S., Hu, W.-F., and Lai, M.-C. A cuspcapturing PINN for elliptic interface problems. *Journal of Computational Physics*, 491:112359, October 2023. ISSN 0021-9991. doi: 10.1016/j.jcp.2023.112359.
- Uhlmann, G. Electrical impedance tomography and Calderón’s problem. *Inverse Problems*, 25(12):123011, December 2009. ISSN 0266-5611. doi: 10.1088/0266-5611/25/12/123011.
- Vogel, C. R. *Computational Methods for Inverse Problems*. Society for Industrial and Applied Mathematics, 2002. doi: 10.1137/1.9780898717570.
- Wang, C., Li, S., He, D., and Wang, L. Is \mathcal{L}^2 Physics Informed Loss Always Suitable for Training Physics Informed Neural Network? In *Advances in Neural Information Processing Systems*, May 2022.
- Wang, S., Teng, Y., and Perdikaris, P. Understanding and Mitigating Gradient Flow Pathologies in Physics-Informed Neural Networks. *SIAM Journal on Scientific Computing*, 43(5):A3055–A3081, January 2021a. ISSN 1064-8275. doi: 10.1137/20M1318043.
- Wang, S., Wang, H., and Perdikaris, P. Learning the solution operator of parametric partial differential equations with physics-informed DeepONets. *Science Advances*, 7(40):eabi8605, September 2021b. doi: 10.1126/sciadv.abi8605.
- Wang, S., Sankaran, S., Wang, H., and Perdikaris, P. An Expert’s Guide to Training Physics-informed Neural Networks, August 2023.
- Wang, S., Li, B., Chen, Y., and Perdikaris, P. PirateNets: Physics-informed Deep Learning with Residual Adaptive Networks, February 2024.

- White, C., Berner, J., Kossaifi, J., Elleithy, M., Pitt, D., Leibovici, D., Li, Z., Azizzadenesheli, K., and Anandkumar, A. Physics-Informed Neural Operators with Exact Differentiation on Arbitrary Geometries. In *The Symbiosis of Deep Learning and Differential Equations III*, October 2023.
- Wu, C., Zhu, M., Tan, Q., Kartha, Y., and Lu, L. A comprehensive study of non-adaptive and residual-based adaptive sampling for physics-informed neural networks. *Computer Methods in Applied Mechanics and Engineering*, 403:115671, January 2023. ISSN 0045-7825. doi: 10.1016/j.cma.2022.115671.
- Yang, L., Meng, X., and Karniadakis, G. E. B-PINNs: Bayesian physics-informed neural networks for forward and inverse PDE problems with noisy data. *Journal of Computational Physics*, 425:109913, January 2021a. ISSN 0021-9991. doi: 10.1016/j.jcp.2020.109913.
- Yang, L., Liu, S., Meng, T., and Osher, S. J. In-context operator learning with data prompts for differential equation problems. *Proceedings of the National Academy of Sciences*, 120(39):e2310142120, September 2023a. doi: 10.1073/pnas.2310142120.
- Yang, Y., Gao, A. F., Castellanos, J. C., Ross, Z. E., Azizzadenesheli, K., and Clayton, R. W. Seismic Wave Propagation and Inversion with Neural Operators. *The Seismic Record*, 1(3):126–134, November 2021b. ISSN 2694-4006. doi: 10.1785/0320210026.
- Yang, Y., Gao, A. F., Azizzadenesheli, K., Clayton, R. W., and Ross, Z. E. Rapid Seismic Waveform Modeling and Inversion With Neural Operators. *IEEE Transactions on Geoscience and Remote Sensing*, 61:1–12, 2023b. ISSN 1558-0644. doi: 10.1109/TGRS.2023.3264210.
- Ye, M., Liu, B., Wright, S., Stone, P., and Liu, Q. BOME! Bilevel Optimization Made Easy: A Simple First-Order Approach, September 2022.
- Yu, J., Lu, L., Meng, X., and Karniadakis, G. E. Gradient-enhanced physics-informed neural networks for forward and inverse PDE problems. *Computer Methods in Applied Mechanics and Engineering*, 393:114823, April 2022. ISSN 0045-7825. doi: 10.1016/j.cma.2022.114823.
- Zhang, R. Z., Ezhov, I., Balcerak, M., Zhu, A., Wiestler, B., Menze, B., and Lowengrub, J. Personalized Predictions of Glioblastoma Infiltration: Mathematical Models, Physics-Informed Neural Networks and Multimodal Scans, January 2024a.
- Zhang, Y., Khanduri, P., Tsaknakis, I., Yao, Y., Hong, M., and Liu, S. An Introduction to Bi-level Optimization: Foundations and Applications in Signal Processing and Machine Learning, December 2023.
- Zhang, Z., Zou, Z., Kuhl, E., and Karniadakis, G. E. Discovering a reaction–diffusion model for Alzheimer’s disease by combining PINNs with symbolic regression. *Computer Methods in Applied Mechanics and Engineering*, 419:116647, February 2024b. ISSN 0045-7825. doi: 10.1016/j.cma.2023.116647.
- Zhou, T., Wan, X., Huang, D. Z., Li, Z., Peng, Z., Anandkumar, A., Brady, J. F., Sternberg, P. W., and Daraio, C. AI-aided geometric design of anti-infection catheters. *Science Advances*, 10(1):eadj1741, January 2024. doi: 10.1126/sciadv.adj1741.
- Zou, Z., Meng, X., and Karniadakis, G. E. Correcting model misspecification in physics-informed neural networks (PINNs). *Journal of Computational Physics*, pp. 112918, March 2024. ISSN 0021-9991. doi: 10.1016/j.jcp.2024.112918.

Impact Statement

This paper presents work whose goal is to advance the field of Machine Learning. There are many potential societal consequences of our work, none which we feel must be specifically highlighted here.

A. Details for Inferring Unknown Functions

As outlined in Section 2.2, suppose f and u are parameterized by neural networks: $f(\mathbf{x}; V)$ and $u(\mathbf{x}; W)$. The data loss is similar to the parameter inference case (3) and depends on both V and W . We also need the regularization loss, evaluated on \mathcal{T}_{reg} :

$$\mathcal{L}_{\text{reg}}(V) = \frac{1}{|\mathcal{T}_{\text{reg}}|} \sum_{\mathbf{x} \in \mathcal{T}_{\text{reg}}} |\nabla_{\mathbf{x}} f(\mathbf{x}; V)|^2. \quad (12)$$

We define the residual loss:

$$\mathcal{L}_{\text{res}}(W, V) := \frac{1}{|\mathcal{T}_{\text{res}}|} \sum_{\mathbf{x} \in \mathcal{T}_{\text{res}}} |a(\mathbf{x}, f(\mathbf{x}; V); W)|^2. \quad (13)$$

and the residual-gradient loss:

$$\mathcal{L}_{\text{rgrad}}(W, V) = \frac{1}{|\mathcal{T}_{\text{res}}|} \sum_{\mathbf{x} \in \mathcal{T}_{\text{res}}} |\nabla_z a(\mathbf{x}, f(\mathbf{x}; V); W)|^2 \quad (14)$$

This has the same interpretation as the parameter inference case (5): small variation of f should lead to small variation of the residual. Finally, we solve the following bilevel optimization problem:

$$\begin{cases} V^* = \arg \min_V \mathcal{L}_{\text{dat}}(W^*(V), V) + w_{\text{reg}} \mathcal{L}_{\text{reg}}(V) & (15) \\ W^*(V) = \arg \min_W \mathcal{L}_{\text{LO}}(W, V) & (16) \end{cases}$$

where $\mathcal{L}_{\text{LO}} = \mathcal{L}_{\text{res}} + w_{\text{rgrad}} \mathcal{L}_{\text{rgrad}}$. At the upper level, we minimize the data loss and the regularization loss with respect to the weights V of the unknown function, and at the lower level, we minimize the local operator loss with respect to the weights W of the local operator. The pre-training stage is similar to the parameter inference case. Given an initial guess of the unknown function f_0 , and its corresponding numerical solution u_0 , we can train the network f_V to approximate f_0 by minimizing the MSE between f_V and f_0 , and train the network u_W to be the local operator at f_0 by minimizing the local operator loss and the MSE between u_W and u_0 .

B. Network Architecture

The network architecture involves a simple modification at the input layer (embedding layer) of the typical fully connected neural network. For the scalar parameter case, the

input layer maps the inputs \mathbf{x} and the unknown PDE parameters Θ to a high-dimensional vector \mathbf{y} , using an affine transformation followed by a non-linear activation function σ :

$$\mathbf{y} = \sigma(W\mathbf{x} + R\Theta + \mathbf{b}), \quad (17)$$

where W is the embedding matrix for \mathbf{x} , R is the embedding matrix for Θ , and \mathbf{b} is the bias vector. The key is that the embedding matrix R should be non-trainable. Otherwise, $\mathcal{L}_{\text{rgrad}}(W, \Theta)$ can be made 0 by setting R to be 0. In our work, R will be randomly initialized in the same way as W , using uniform distributions in the range of $[-1/\sqrt{d}, 1/\sqrt{d}]$, where d is the number of input units in the layer. The embedding vector \mathbf{y} is then passed through a series of fully connected layers with activation functions. The output of the network is denoted as $\mathcal{N}(\mathbf{x}, \Theta; W)$, where W denotes all the trainable weights of the neural network. In some cases, a final transformation is applied to the output of the neural network $u(\mathbf{x}; W) = \tau(\mathcal{N}(\mathbf{x}, \Theta; W), \mathbf{x})$, to enforce the boundary condition (Dong & Ni, 2021; Lu et al., 2021c; Sukumar & Srivastava, 2022).

C. Proof of Theorem 2.1

In the main text, we describe the simultaneous gradient descent algorithm for the bi-level optimization problem. In this section, we provide a justification of the algorithm under some assumptions.

We consider the boundary value problem:

$$\begin{cases} \mathbf{L}u = f & \text{in } \Omega \\ u = g & \text{on } \partial\Omega, \end{cases} \quad (18)$$

where Ω is an connected, open and bounded subset of \mathbb{R}^d . \mathbf{L} denoted a second-order parital differential operator:

$$\mathbf{L}u = \sum_{i,j=1}^d a_{ij} \partial_{ij} u + \sum_{i=1}^d b_i \partial_i u + cu \quad (19)$$

where the coefficients a_{ij} , b_i , c are colletively denoted as Θ . We denote \mathbf{L}_{Θ} as the derivative of \mathbf{L} with respect to Θ , which is also a differential operator.

We say a function $u(\mathbf{x}, \Theta)$ is a local solution operator of the PDE (19) at Θ if (1) $\mathbf{L}u = f$ and (2) $L_{\Theta}u + L\nabla_{\Theta}u = 0$. That is, the residual at Θ is zero and the gradient of the residual w.r.t Θ is zero.

We consider a parameterized local operator $u(\mathbf{x}, \Theta; W)$. For notational simplicity, we omit the dependence of u on \mathbf{x} in the following discussion and the dependence of W^* on Θ (but W is not a functon of Θ). We assume that $u(\Theta; W) = g$ on $\partial\Omega$ for all W and Θ .

Our bilevel optimizaiton problem is

$$\min_{\Theta} \int_{\Omega} (u(\Theta, W^*) - \hat{u})^2 d\mathbf{x}$$

$$W^* = \arg \min \int_{\Omega} (\mathbf{L}u - f)^2 + w_{\text{reg}} (L_{\Theta}u + L\nabla_{\Theta}u)^2 dx$$

where $\mathbf{L}u - f$ is the residual of the PDE, and $L_{\Theta}u + L\nabla_{\Theta}u$ is the gradient of the residual w.r.t Θ .

In our simultaneous gradient descent, the gradient of the upper level objective with respect to Θ is given by

$$g_a(W, \Theta) = \int_{\Omega} (u(W, \Theta) - \hat{u}) (\nabla_{\Theta}u(W, \Theta)) dx \quad (20)$$

The exact gradient of the upper level objective is

$$g(\Theta) = \int_{\Omega} (u(W^*, \Theta) - \hat{u}) (\nabla_W u(W^*, \Theta) \nabla_{\Theta} W^* + \nabla_{\Theta} u(W^*, \Theta)) dx \quad (21)$$

At W^* , the difference between the exact gradient and the approximate gradient, which we denote as Δg , is given by

$$\begin{aligned} \Delta g(\Theta) &:= g_a(W^*, \Theta) - g(\Theta) \\ &= \int_{\Omega} (u(W^*, \Theta) - \hat{u}) (\nabla_W u(W^*, \Theta) \nabla_{\Theta} W^*) dx \end{aligned} \quad (22)$$

Suppose the lower level problem has a minimizer W^* such that the $u(W^*, \Theta)$ is the local operator.

$$\mathbf{L}u(W^*, \Theta) - f = 0 \quad (23)$$

and

$$\mathbf{L}_{\Theta}u(W^*, \Theta) + \mathbf{L}\nabla_{\Theta}u(W^*, \Theta) = 0 \quad (24)$$

Take the derivative of the Eq. (23) with respect to Θ , we have

$$\mathbf{L}_{\Theta}u(W^*, \Theta) + \mathbf{L}\nabla_{\Theta}u(W^*, \Theta) + \mathbf{L}\nabla_W u(W^*, \Theta) \nabla_{\Theta} W^* = 0 \quad (25)$$

From Eq. (24) and Eq. (25), we have

$$\mathbf{L}\nabla_W u(W^*, \Theta) \nabla_{\Theta} W^* = 0 \quad (26)$$

We denote the function $v := \nabla_W u(W^*, \Theta) \nabla_{\Theta} W^*$. Since $u(W, \Theta) = g$ on $\partial\Omega$ for all W and Θ , we have $v = 0$ on $\partial\Omega$. Therefore, we have $\mathbf{L}v = 0$ in Ω and $v = 0$ on $\partial\Omega$. If the maximum principal holds for the operator \mathbf{L} , for example, when \mathbf{L} uniformly elliptic and $c \geq 0$, (Evans, 2010) then we have $v = 0$.

By Cauchy-Schwarz inequality, we have

$$\|\Delta g\|_2 \leq \|u(W^*, \Theta) - \hat{u}\|_2 \|v\|_2 = 0 \quad (27)$$

That is, the approximate gradient at $W^*(\Theta)$ is exact.

The assumptions are more restrictive than the numerical experiments. For example, in the Fisher-KPP example, the PDE operator is nonlinear. A more comprehensive and general analysis is left for future work, for example, bounding the error of the approximate gradient by the lower level optimization error (Pedregosa, 2022).

D. Training Details and Additional Results

For each numerical experiment, we solve the optimization problem 5 times with different random seed. which affect both the initialization of the neural network and the noise in the data (if applicable). Although each realization of the noise may yield a different optimal parameter Θ^* , the average of the optimal parameters across multiple runs should still be close to the ground truth parameter Θ_{GT} . Therefore, we report the mean and standard deviation of the error between the inferred parameters, or functions, and the ground truth quantities.

In all the numerical experiment, we use the tanh activation function and 2 hidden layers, each with 128 neurons, for both PINN and BiLO. The collocation points are evenly spaced as a grid in the domain. For all the optimization problems, we use the Adam optimizer with learning rate 0.001 and run a fixed number of steps.

D.1. Fisher-KPP Equation

Our local operator take the form of $u(x, t, D, \rho; W) = u(x, 0) + \mathcal{N}(x, t, D, \rho; W)x(1-x)t$ so that the initial condition and the boundary condition are satisfied. Let X_r, X_d be the spatial coordinates evenly spaced in $[0, 1]$, and T_r be temporal coordinates evenly spaced in $[0, 1]$. We set $\mathcal{T}_{\text{res}} = X_r \times T_r$ and $|X_r| = |T_r| = 51$, that is, the residual collocation points are a uniform grid in space and time. We set $\mathcal{T}_{\text{dat}} = X_d \times \{1\}$ and $|X_d| = 11$, that is, the data collocation points form a uniform grid at the final time $t = 1$. Both BiLO and PINN are pretrained with the initial guess for 10,000 steps, and fine-tuned for 50,000 steps.

In Fig. 8, we show the training history of the inferred parameters and the inferred parameters, and indicate the ground truth with grey dashed line. In Fig. 9, we show the history of the losses of BiLO. The data are collected every 20 steps and we applied a moving average with window size 10 to smooth the curves.

D.1.1. VISUALIZATION OF LOCAL OPERATOR

We consider the case without noise and show the trajectories of the parameters D and ρ during the fine-tuning process in Fig. 10. Each BiLO trajectory (black line) corresponds to a different random initialization of the neural network, and are obtained by our simultaneous gradient descent. They roughly follow the trajectory that is obtained

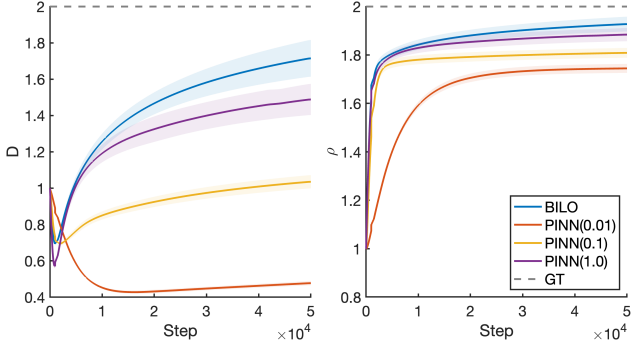


Figure 8: Training history of the inferred parameters corresponding for BiLO and PINN (with various w_{dat}) for the Fisher-KPP equation with $\sigma = 0.01$. The solid line is the mean of the inferred parameters across 5 runs, and the shaded region indicates the standard deviation.

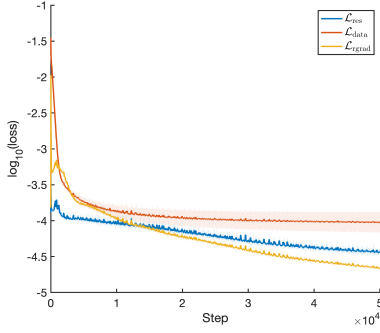


Figure 9: Training history of the unweighted losses (\mathcal{L}_{res} , \mathcal{L}_{dat} , and $\mathcal{L}_{\text{rgrad}}$) during the fine-tuning stage for solving inverse problems using BiLO for the Fisher-KPP equation (Section 3.1, $\sigma = 0.01$). Solid lines are the mean of the losses across 5 runs, and the shaded regions indicate the standard deviation.

by solving the lower level problem to a small tolerance before updating the PDE parameters (red dashed line). The contours are the data loss in log scale using the FDM solution for each parameter pair (D, ρ) . Note that the contour lines do not represent the actual loss landscape of our optimization problem, since at each step we are not solving the PDE to high accuracy. From the landscape we can also see that single-time inference is challenging, as the gradient with respect to D is much smaller than ρ , leading to a narrow valley in the loss landscape along the D -direction.

D.1.2. COMPARISON WITH NEURAL OPERATORS

We explain the setup for the comparison between BiLO and NO in Section 3.1. For the NO, we use the DeepONet architecture (Lu et al., 2021a) as an example, which is shown to have comparable performance with FNO (Li et al., 2021; Lu et al., 2022a). It is difficult to directly compare the per-

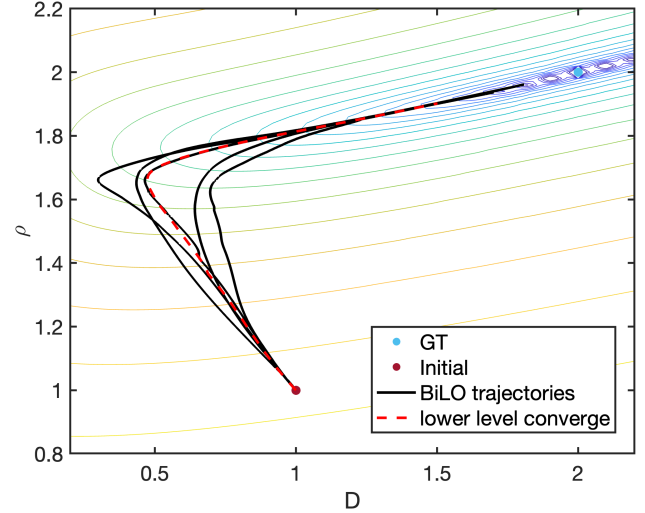


Figure 10: Trajectory of the parameters D and ρ during fine-tuning roughly follow the path of the steepest descent.

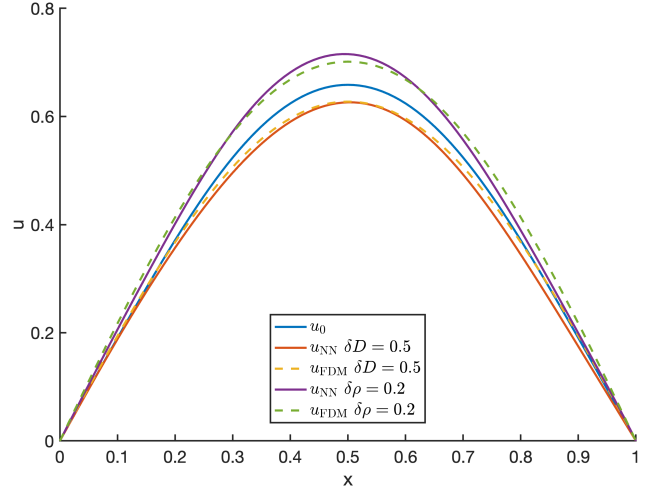


Figure 11: Evaluating the local operator $u(\mathbf{x}, D_0 + \delta D, \rho_0 + \delta \rho)$ at $t = 1$ after pretraining at D_0 and ρ_0 , approximate the corresponding FDM solutions.

formance of NO and PINN/BiLO, since NOs are designed to learn the solution operator of the PDE, while both the PINN and BiLO can be considered as the solver of the PDE, which solve the PDE for one set of parameters. Usually, NO is trained with a large amount of numerical solutions. In this experiment, for solving the inverse problem, we first train the NO, and then we use the NO as a surrogate and use gradient-based optimization to infer the parameters of the PDE. We show that the quality of the inferred parameters depends on the synthetic data used to train the NO. We emphasize that NO can excel in multi-query scenarios, such as solving the inverse problem in a Bayesian framework, which requires evaluating the solution of the PDE

for many different parameters.

We consider the following 2 datasets for pretraining the DeepONet. The ground truth parameters are $D_{GT} = 2$ and $\rho_{GT} = 2$, and the initial guess is $D_0 = 1$ and $\rho_0 = 1$. The PDE parameters are sampled with different range and different resolution. We use the notation $a : h : b$ to denote an array from a to b with step h .

- Coarse: $D = 0.8 : 0.05 : 3, \rho = 0.8 : 0.05 : 3$.
- Dense: $D = 0.8 : 0.02 : 3, \rho = 0.8 : 0.02 : 3$.

In the ‘‘Coarse’’ dataset, the parameters are sampled with a larger step size. In the ‘‘Dense’’ dataset, the parameters are sampled with a smaller step size.

We use the following architecture for the DeepONet:

$$G_W(D, \rho, \mathbf{x}) = \sum_{i=1}^k b_k(D, \rho) t_k(\mathbf{x})$$

where $b_k(D, \rho)$ is the k -th output of the ‘‘branch net’’, and $t_k(\mathbf{x})$ is the k -th output of the ‘‘trunk net’’. Both the trunk net and the truck net are parameterized by fully neural networks with 2 hidden layers, each with 128 neurons, so that the total number of parameters (46179) are comparable to the network used by BiLO (42051). The weights of the DeepONet are denoted as W . A final transformation on the output G_W is used to enforce the boundary condition. We pre-train multiple DeepONets with 10,000 steps using each datasets.

Given a pretrain dataset with collections of $\{D^j, \rho^j\}$ and their corresponding solutions u^j for $j = 1, \dots, m$, we first train the DeepONet with the following operator data loss:

$$\min_W \sum_{j=1}^m \sum_{\mathbf{x} \in \mathcal{T}_{\text{dat}}} |G_W(D^j, \rho^j, \mathbf{x}) - u^j(\mathbf{x})|^2$$

where \mathcal{T}_{dat} is the same as those used in the BiLO and PINN. For the inverse problem, we fix the weights W and treat the D and ρ as unknown variables. We minimize the data loss:

$$\min_{D, \rho} \frac{1}{|\mathcal{T}_{\text{dat}}|} \sum_{\mathbf{x} \in \mathcal{T}_{\text{dat}}} |G_W(D, \rho, \mathbf{x}) - \hat{u}(\mathbf{x})|^2$$

where \hat{u} is the noisy data.

D.2. Inferring Stochastic Rates from Particle Positions

The equation can be written as the elliptic interface problem:

$$\begin{cases} \Delta u - \mu u = 0 \\ u(0) = u(1) = 0 \\ u^+(z) = u^-(z) \\ u_x^+(z) - u_x^-(z) = -\lambda \end{cases} \quad (28)$$

where the superscript $+$ and $-$ denote the values on the right and left side of the interface, respectively. For the cusp-capturing PINN, we search for function $U(x, \phi)$ such that $u(x) = U(x, |x - z|)$. The continuity condition is satisfied, and the jump condition translate to $\partial_\phi U(z, 0) = -\lambda$. The cusp-capturing PINN is parameterized by $U(x, \phi; W)$, and to enforce the jump condition, we need the ‘‘jump loss’’:

$$\mathcal{L}_{\text{jump}} = \partial_\phi U(z, 0; W)^2$$

In the BiLO framework, the local operator is parameterized as $U(x, \phi, \lambda, \mu; W)$, and the jump condition also requires the gradient of the jump condition with respect to λ and μ to be zero. Therefore, we need the ‘‘jump gradient loss’’:

$$\mathcal{L}_{\text{jgrad}} = \partial_\lambda \partial_\phi U(z, 0, \lambda, \mu; W)^2 + \partial_\mu \partial_\phi U(z, 0, \lambda, \mu; W)^2$$

D.3. Variable-Diffusion Coefficient Poisson Equation

The local operator takes the form of $u(x, z; W) = \mathcal{N}_1(x, z; W)x(1 - x)$ to enforce the boundary condition, where the fully connected neural network \mathcal{N}_1 has 2 hidden layers, each with 128 neurons. The unknown function is parameterized by $D(x; V) = \mathcal{N}_2(x, V)x(1 - x) + 1$, where \mathcal{N}_2 has 2 hidden layers, each with 64 neurons. For pre-training, we set $|\mathcal{T}_{\text{res}}| = |\mathcal{T}_{\text{reg}}| = |\mathcal{T}_{\text{dat}}| = 101$, and train 10,000 steps. For fine-tuning, we set $|\mathcal{T}_{\text{res}}| = |\mathcal{T}_{\text{reg}}| = 101$ and $|\mathcal{T}_{\text{dat}}| = 51$, and train 10,000 steps. In Fig. 12, we show the training history of the ℓ_2 error of the inferred $D(x)$ for BiLO and PINN (with various w_{dat}).

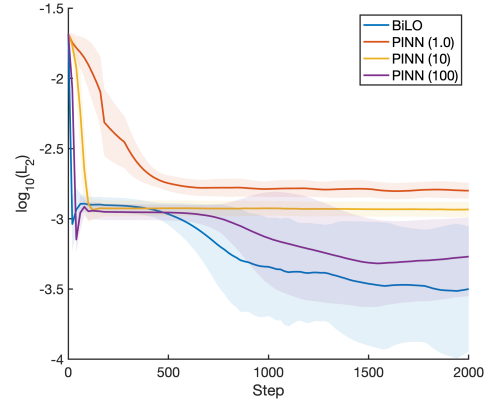


Figure 12: Training history (first 2000 steps) of the L_2 error of the inferred $D(x)$ in log scale.

In Fig. 13, we visualize the local operator $u(x, z; W)$ after pre-training with $D_0(x) = 1$. We consider the variation $\delta D_1(x) = -0.1$, and $\delta D_2(x) = 0.1x$ and evaluate the neural network at $u(x, D_0(x) + \delta D_i(x); W)$ for $i = 1, 2$. The FDM solutions of the PDE corresponding to $D_0(x) + \delta D_i(x)$ are also plotted. We can see that the neural network approximates the solution corresponding to $D_0(x) + \delta D_i(x)$ well.

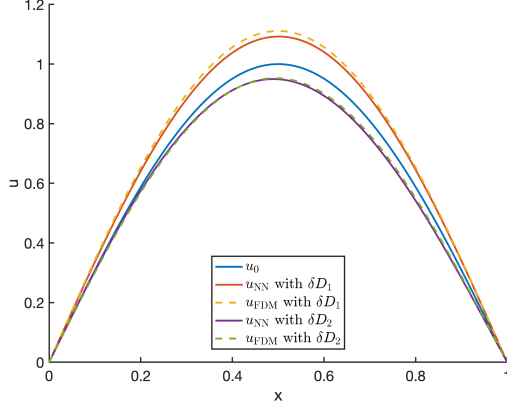


Figure 13: Visualizing the operator $u(x, D(x) + \delta D(x); W)$ after pre-training with $D_0(x) = 1$.

D.3.1. IMPLEMENTATION OF THE ADJOINT METHODS

For the numerical example on learning the variable diffusion coefficient of the Poisson Equation, we implement the adjoint method following Vogel (2002). The domain is discretized with uniformly spaced grid points: $x_i = hi$ for $i = 0, \dots, n, n+1$, where h is the spacing of the grid points and n is the number of intervals. We use the finite element discretization with linear basis functions ϕ_i . Let \mathbf{u} be the nodal value of the solution u at x_i for $i = 1, \dots, n$ and similar for \mathbf{D} . We have $\mathbf{u}_0 = \mathbf{u}_{n+1} = 0$ and $\mathbf{D}_0 = \mathbf{D}_{n+1} = 1$. The stiffness matrix $A(\mathbf{D})$ is given by

$$A(\mathbf{D})_{ij} = \frac{1}{2} \begin{cases} \mathbf{D}_{i-1} + 2\mathbf{D}_i + \mathbf{D}_{i+1} & \text{if } i = j \\ -(\mathbf{D}_i + \mathbf{D}_j) & \text{if } |i - j| = 1 \\ 0 & \text{otherwise} \end{cases} \quad (29)$$

The load vector \mathbf{f} is given by $\mathbf{f}_i = f(x_i)$. Suppose the observed data is located at some subset of the grid points of size m . Then $\hat{\mathbf{u}} = C\mathbf{u} + \eta$, where η is the noise, and $C \in \mathbb{R}^{m \times n}$ is the observation operator. After discretization, the minimization problem is

$$\begin{aligned} \min_{\mathbf{D}} \|\mathbf{C}\mathbf{u} - \hat{\mathbf{u}}\|_2^2 + \frac{w_{\text{reg}}}{2} \sum_{i=1}^N (\mathbf{D}_{i+1} - \mathbf{D}_i)^2 \\ \text{s.t. } A(\mathbf{D})\mathbf{u} = \mathbf{f} \end{aligned}$$

The gradient of the loss function with respect to the diffusion coefficient is given by

$$\mathbf{g}_i = \left\langle \frac{\partial A}{\partial \mathbf{D}_i} \mathbf{u}, \mathbf{z} \right\rangle + w_{\text{reg}} (\mathbf{D}_{i+1} - 2\mathbf{D}_i + \mathbf{D}_{i-1})$$

where \mathbf{z} is the solution of the adjoint equation $A^T \mathbf{z} = C^T (C\mathbf{u} - \hat{\mathbf{u}})$. Gradient descent with step size 0.1 is used to update D , and is stopped when the norm of the gradient is less than 10^{-6} .

In table 2, we show the full results of the numerical experiments in Section 3.3 in the main text, with $w_{\text{reg}} = 1e-2, 1e-3, 1e-4$.

D.3.2. COMPARISON WITH DEEPONET

In this experiment, we infer the variable diffusion coefficient $D(x)$ in the Poisson equation using a DeepONet. The pretrain dataset is generated by solving the Poisson equation with 1000 samples of variable diffusion coefficient $D(x)$. $D(x)$ is sampled from a Gaussian Random field on $[0, 1]$, conditioned on $D(0) = D(1) = 1$. The covariance function is the gaussian kernel, with variance 0.05 and different length scale $l = 0.2, 0.3, 0.4$. See Figure 14 for the samples of $D(x)$ and their corresponding solutions. As l increases, the samples of $D(x)$ become smoother.

The DeepONet has the following architecture:

$$G_W(\mathbf{D}, \mathbf{x}) = \sum_{i=1}^k b_k(\mathbf{D}) t_k(\mathbf{x})$$

where the vector \mathbf{D} represent the values of $D(x)$ at the collocation points. A final transformation on the output G_W is used to enforce the boundary condition. In this experiment, both D and u are evaluated at 101 points in $[0, 1]$. Let x_i be the collocation points in $[0, 1]$ for $i = 1 = 0, \dots, N$. Let $\{D^j(x_i), u^j(x_i)\}$ be the samples of D and the corresponding solutions u at x_i for $j = 1, \dots, m$. We denote \mathbf{D}^j as the vector of $D^j(x_i)$ for $i = 0, \dots, N$. In the pre-training step, we solve the following minimization problem

$$\min_W \sum_{j=1}^m \sum_{i=1}^N |G_W(\mathbf{D}^j, x_i) - u^j(x_i)|^2$$

For the inverse problem, we fix the weights W and treat the \mathbf{D} as an unknown variable. We minimize the data loss and a finite difference discretizations of the regularization term $|D(x)|^2$:

$$\begin{aligned} \min_{\mathbf{D}} \frac{1}{N} \sum_{i=1}^N |G_W(\mathbf{D}, x_i) - \hat{u}(x_i)|^2 + \\ w_{\text{reg}} \sum_{i=0}^N |(\mathbf{D}_{i+1} - \mathbf{D}_i)/h|^2 \end{aligned}$$

where h is the spacing of the collocation points, $\mathbf{D}_0 = \mathbf{D}_N = 1$. Here we work with the vector \mathbf{D} for simplicity. Alternatively, we can represent $D(x)$ as a neural network as in PINN and BiLO experiments.

We perform a grid search on the hyperparameters $l = 0.1, 0.2, 0.3, 0.4$ and $w_{\text{reg}} = 1e-3, 1e-4, 1e-5$. In Table 3, we show the 3 combinations of l and w_{reg} with the best performance in terms of the L_2 error of the inferred $D(x)$ and

method	$\ D - D_{GT}\ _\infty$	$\ D - D_{GT}\ _2$	$\ u_{NN} - u_{FDM}\ _\infty$	$\mathcal{L}_{\text{data}}$
BiLO(1e-2)	1.08e-1±3.92e-3	4.88e-2±2.18e-3	2.07e-2±1.28e-3	2.57e-4±2.01e-5
BiLO(1e-3)	5.86e-2±1.99e-2	2.01e-2±7.94e-3	3.94e-3±1.93e-3	1.01e-4±1.80e-5
BiLO(1e-4)	7.53e-2±1.54e-2	2.88e-2±7.91e-3	4.30e-3±1.42e-3	9.59e-5±1.79e-5
Adjoint(1e-2)	12.4e-2±3.35e-2	5.53e-2±1.45e-2	-	8.05e-5±1.29e-5
Adjoint(1e-3)	7.89e-2±2.27e-2	3.12e-2±9.00e-3	-	9.14e-5±1.54e-5
Adjoint(1e-4)	1.09e-1±7.01e-3	4.29e-2±3.95e-3	-	1.03e-4±1.73e-5
PINN(1e-2/1e0)	1.62e-1±4.90e-3	7.91e-2±2.88e-3	3.05e-2±1.46e-3	3.85e-4±2.19e-5
PINN(1e-2/1e1)	1.17e-1±7.67e-3	4.83e-2±3.92e-3	8.16e-3±1.64e-3	1.14e-4±1.97e-5
PINN(1e-2/1e2)	8.69e-2±1.76e-2	3.31e-2±7.99e-3	4.18e-3±1.80e-3	1.02e-4±1.21e-5
PINN(1e-3/1e0)	9.99e-2±2.88e-3	3.97e-2±1.73e-3	6.37e-3±1.54e-3	1.09e-4±1.85e-5
PINN(1e-3/1e1)	8.61e-2±7.50e-3	3.25e-2±3.96e-3	4.43e-3±1.37e-3	1.02e-4±1.87e-5
PINN(1e-3/1e2)	7.13e-2±1.59e-2	3.11e-2±1.09e-2	4.88e-3±1.45e-3	9.42e-5±1.55e-5
PINN(1e-4/1e0)	8.69e-2±5.54e-3	3.25e-2±2.94e-3	4.49e-3±9.97e-4	1.04e-4±1.86e-5
PINN(1e-4/1e1)	7.13e-2±2.08e-2	2.64e-2±8.09e-3	4.23e-3±1.15e-3	9.88e-5±1.72e-5
PINN(1e-4/1e2)	7.51e-2±2.02e-2	3.52e-2±1.45e-2	5.19e-3±1.44e-3	9.35e-5±1.51e-5

Table 2: Comparison of BiLO (with various w_{reg}), Adjoint Method (with various w_{reg}), and PINN (with various $w_{\text{reg}}/w_{\text{dat}}$)

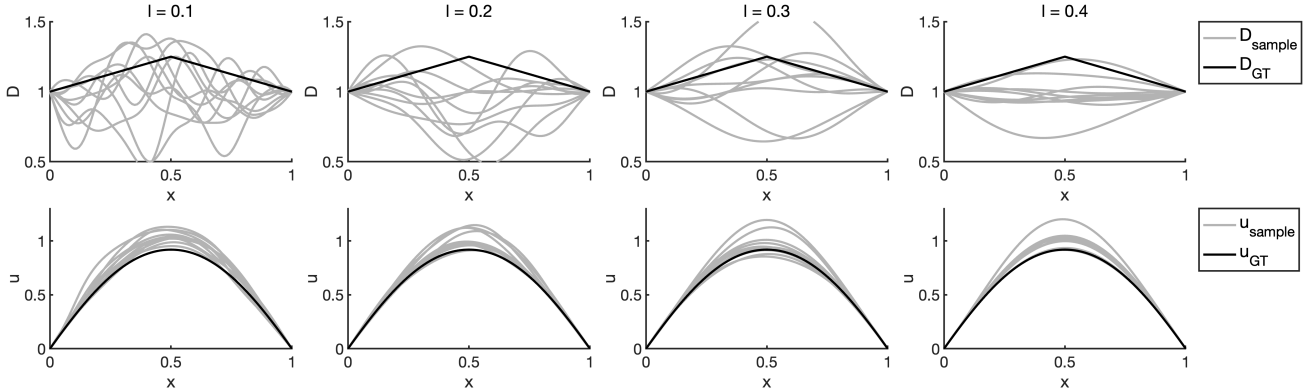


Figure 14: Samples (gray lines) of $D(x)$ with various length scale l and their corresponding solutions. Black line is the ground truth D and u

the ground truth. As shown in Table 3, the performance of the inference depends on properties of the pre-training dataset. In practice, it might be difficult to know what does the ground truth unknown function look like. This highlights the importance of the residual loss used in BiLO and PINN, which can help to learn the solution of the PDE without prior knowledge of the ground truth solution.

D.4. Infer the Initial Condition of a Heat Equation

In this example, we aim to infer the initial condition of a 1D heat equation from the final state. Consider the heat equation

$$\begin{cases} u_t(x, t) = Du_{xx}(x, t) \\ u(x, 0) = f(x) \\ u(0, t) = u(1, t) = 0 \end{cases} \quad (30)$$

on $x \in [0, 1]$ and $t \in [0, 1]$, with fixed diffusion coefficient $D = 0.01$, and unknown initial condition $f(x)$, where $f(0) = f(1) = 0$. Our goal is to infer the initial condition $f(x)$ from observation of the final state $u(x, 1)$. We set the ground truth initial condition f_{GT} to be the hat function

$$f_{GT}(x) = \begin{cases} 2x, & \text{if } x \in [0, 0.5] \\ 2 - 2x, & \text{if } x \in [0.5, 1] \end{cases} \quad (31)$$

We set the initial guess $f_0(x) = \sin(\pi x)$. We can represent the unknown function $f(x; V) = s(\mathcal{N}(x; V))x(1-x)$, where \mathcal{N}_f is a fully connected neural network with 2 hidden layers and width 64, and s is the softplus activation function (i.e., $s(x) = \log(1 + \exp(x))$). The transformation ensures that the initial condition satisfies the boundary condition and is non-negative. For BiLO, the neural network is represented as $u(x, t, z) = N_u(x, t, z; W)x(1-x)t + z$, where N_u is a fully connected neural network with 2

method	$\ D - D_{GT}\ _\infty$	$\ D - D_{GT}\ _2$	$\ u_{\text{NN}} - u_{\text{FDM}}\ _\infty$	$\mathcal{L}_{\text{data}}$
BiLO	5.86e-2±1.99e-2	2.01e-2±7.94e-3	3.94e-3±1.93e-3	1.01e-4±1.80e-5
DeepONet(0.2/1e-5)	5.55e-2±7.99e-3	2.36e-2±2.05e-3	6.56e-3±2.36e-3	9.45e-5±1.47e-5
DeepONet(0.4/1e-5)	6.83e-2±2.76e-2	2.94e-2±1.14e-2	8.65e-3±9.37e-4	8.62e-5±1.36e-5
DeepONet(0.4/1e-4)	8.22e-2±2.08e-2	3.16e-2±8.63e-3	7.73e-3±1.89e-3	1.01e-4±1.83e-5

Table 3: Comparison of BiLO and DeepONets (l / w_{reg}) pre-trained with datasets with different length scale l and regularization weight w_{reg} .

hidden layers and width 128. For the PINN, we have $u(x, t; W, V) = N_u(x, t; W)x(1-x)t + f(x; V)$. These transformations ensure that the networks satisfy the boundary and initial condition.

Let X_r, X_d be spatial coordinates evenly spaced in $[0, 1]$ and T_r be temporal coordinates evenly spaced in $[0, 1]$ (both including the boundary). We set $\mathcal{T}_{\text{res}} = X_r \times T_r$ and $|X_r| = |T_r| = 51$. That is, the residual collocation points is a uniform grid in space and time. We set $\mathcal{T}_{\text{dat}} = X_d \times \{1\}$ and $|X_d| = 11$. That is, the data collocation points is a uniform grid in space at the final time $t = 1$. We set the collocation point for the regularization loss of the unknown function \mathcal{T}_{reg} to be 101 evenly spaced points in the spatial domain.

To evaluate the performance of the inferred initial condition f , we use the L_2 norm and the L_∞ norm of the difference between the inferred initial condition and the ground truth initial condition, which are evaluated at 1001 evenly spaced points in the spatial domain.

WITHOUT NOISE

First we consider the case where the data is provided at $t = 1$ without noise. In this case, we also do not use regularization term for the initial condition. In Fig. 15, and Table 4, we show the results of PINNs various weights $w_{\text{dat}} = 0.1, 10, 1000$, and BiLO. We can see that BiLO achieved the best e_2 and e_∞ , demonstrating the effectiveness in recovering the non-smooth initial condition. With very large data loss, the error of the PINN increases. This is because data is only provided at the final time, we need to solve the PDE accurately to infer the initial condition.

WITH NOISE

In this experiment, we consider the case with noise $\epsilon \sim N(0, 0.001)$. Due to the ill-posedness of the inverse problem, we need to regularize the problem by the 2-norm of the derivative of the unknown function with $w_{\text{reg}} = 1e-2$. In Fig. 16 and Table 5, we show examples of the inferred initial condition and the PDE solution for the PINN formulation with various w_{dat} . In Table 5, for the PINN, we can see that as w_{dat} increase from 0.1 to 10, it seems that the reconstruction error decreases. However, the \mathcal{L}_{dat} is

becoming smaller than the variance of the noise, indicating that the PINN is overfitting the data. This can also be observed from the Fig 16, for $w_{\text{dat}} = 1e3$, we see larger discrepancy between u_{PINN} and u_{FDM} .

D.5. Inviscid Burger’s Equation

We consider an inverse problem governed by an inviscid Burger’s equation on the domain $x \in [0, 1]$ and $t \in [0, 1]$.

$$\begin{cases} u_t + auu_x = 0 \\ u(x, 0) = f(x) \\ u(0, t) = u(1, t) = 0 \end{cases} \quad (32)$$

where $a = 0.2$. We aim to infer the initial condition f from the observational data at $t = 1$. The numerical solutions are computed by using the Godunov scheme. The inviscid Burger’s equation is a hyperbolic PDE, and the solution can develop shocks and rarefaction waves.

We present two examples, as shown in Fig. 5 and Fig. 17. In both examples, the initial guess is $f(x) = 1 - \cos(2\pi x)$, which leads to a mostly smooth solution in the time interval $[0, 1]$. In example 1 (Fig 5), the ground truth solution corresponds to the initial condition $f(x) = \sin(2\pi x)$. In example 2 (Fig 17), the ground truth solution corresponds to the initial condition $f(x) = -\cos(2\pi x)$ for $x \in [\pi/4, 3\pi/4]$ and $f(x) = 0$ otherwise. Notice that both solutions develop shocks and rarefaction waves, and thus the solution is non-smooth.

In Fig. 5 and Fig. 17, we show the initial guess in the first column, the ground truth in the second column, and the inference results by BiLO in the third column. The first row shows the initial condition $f(x)$, the second rows shows the solution $u(x, t)$ on the domain $x \in [0, 1]$ and $t \in [0, 1]$, and the thrid row shows the solution $u(x, 1)$. Notice that for inference, only solution at $t = 1$ of the ground truth is provided. We can see that the BiLO can accurately infer the initial condition of the Burger’s equation, even when the solution is non-smooth.

D.6. 2D Darcy Flow

The setup of this experiment is similar to the steady state Darcy flow inverse problem in (Li et al., 2024). Let $\phi(\mathbf{x})$

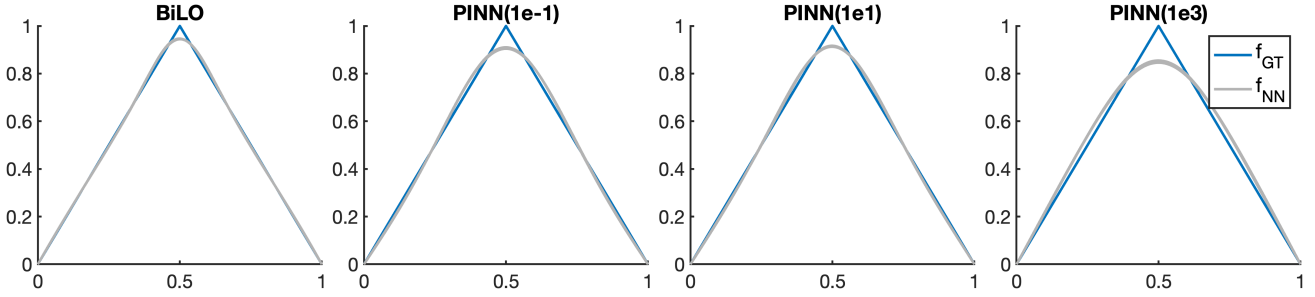
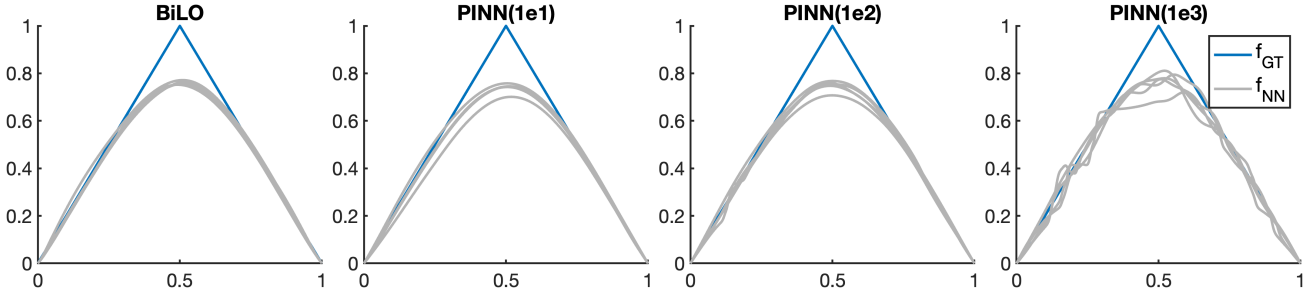


Figure 15: Predicted initial conditions of the heat equation (without noise) from 5 random seeds.

method	$\ f_{\text{NN}} - f_{\text{GT}}\ _{\infty}$	$\ f_{\text{NN}} - f_{\text{GT}}\ _2$	$\ u_{\text{NN}} - u_{\text{FDM}}\ _{\infty}$	$\mathcal{L}_{\text{data}}$
BiLO	$5.43\text{e-}2 \pm 1.00\text{e-}3$	$1.01\text{e-}4 \pm 7.46\text{e-}6$	$4.64\text{e-}4 \pm 2.57\text{e-}4$	$1.52\text{e-}9 \pm 5.89\text{e-}10$
PINN(1e-1)	$9.24\text{e-}2 \pm 2.21\text{e-}3$	$5.43\text{e-}4 \pm 2.81\text{e-}5$	$1.29\text{e-}3 \pm 1.53\text{e-}3$	$4.05\text{e-}6 \pm 4.57\text{e-}6$
PINN(1e1)	$8.69\text{e-}2 \pm 2.39\text{e-}3$	$4.31\text{e-}4 \pm 5.06\text{e-}5$	$2.44\text{e-}3 \pm 9.86\text{e-}4$	$1.62\text{e-}6 \pm 1.82\text{e-}6$
PINN(1e3)	$1.49\text{e-}1 \pm 4.19\text{e-}3$	$1.92\text{e-}3 \pm 1.34\text{e-}4$	$2.54\text{e-}2 \pm 2.92\text{e-}3$	$3.83\text{e-}8 \pm 5.36\text{e-}8$

 Table 4: Comparison of BiLO and PINNs (with various w_{dat}) for inferring the unknown initial condition (without noise), showing mean (std).

 Figure 16: Predicted initial condition $f(x)$ by BiLO and PINNs with various w_{dat} .

method	$\ f_{\text{NN}} - f_{\text{GT}}\ _{\infty}$	$\ f_{\text{NN}} - f_{\text{GT}}\ _2$	$\ u_{\text{NN}} - u_{\text{FDM}}\ _{\infty}$	$\mathcal{L}_{\text{data}}$
BiLO	$2.41\text{e-}1 \pm 7.62\text{e-}3$	$6.11\text{e-}3 \pm 5.36\text{e-}4$	$1.46\text{e-}3 \pm 7.50\text{e-}4$	$4.08\text{e-}3 \pm 2.53\text{e-}4$
PINN(1e1)	$2.62\text{e-}1 \pm 2.22\text{e-}2$	$8.13\text{e-}3 \pm 2.79\text{e-}3$	$1.26\text{e-}1 \pm 3.27\text{e-}2$	$5.21\text{e-}4 \pm 1.55\text{e-}4$
PINN(1e2)	$2.53\text{e-}1 \pm 2.34\text{e-}2$	$7.11\text{e-}3 \pm 2.06\text{e-}3$	$1.38\text{e-}1 \pm 3.17\text{e-}2$	$2.61\text{e-}4 \pm 1.56\text{e-}4$
PINN(1e3)	$2.42\text{e-}1 \pm 4.65\text{e-}2$	$6.56\text{e-}3 \pm 2.70\text{e-}3$	$1.36\text{e-}1 \pm 3.33\text{e-}2$	$2.05\text{e-}4 \pm 1.65\text{e-}4$

 Table 5: Comparison of the BiLO and PINN (with various w_{dat}) for a heat equation with unknown initial condition (noise $\epsilon \sim N(0, 0.001)$), showing mean (std).

be samples of a Gaussian random field (GRF) with mean 0 and squared exponential (Gaussian) covariance structure $C(\mathbf{x}, \mathbf{y}) = \sigma \exp(-\|\mathbf{x} - \mathbf{y}\|^2 / \lambda^2)$, where the marginal standard deviation $\sigma = \sqrt{10}$ and the correlation length $l = 0.01$ (Constantine, 2024). This GRF is different from (Li et al., 2024). We generate the initial guess $A_0(\mathbf{x}) = \text{sigmoid}(\phi_0(\mathbf{x})) \times 9 + 3$, where $\phi_0(\mathbf{x})$ is a sample of the GRF. We consider the ground truth diffusion coefficient to be a piece-wise constant function: $A_{\text{GT}}(\mathbf{x}) = 12$ if $\phi_{\text{GT}}(\mathbf{x}) > 0$ and $A_{\text{GT}}(\mathbf{x}) = 3$ otherwise, where ϕ_{GT} is another sample of the GRF. The corresponding solution of A_0 and A_{GT} are denoted as u_0 and u_{GT} .

We pretrain the BiLO with $A_0(\mathbf{x})$ and its corresponding solution $u_0(\mathbf{x})$ for 10,000 steps. And we fine-tune the BiLO for 5,000 steps using $u_{\text{GT}}(\mathbf{x})$ to infer A_{GT} . Following (Li et al., 2024), we use the total variation regularization $|\nabla A|$ with weight $w_{\text{reg}} = 1e - 9$.

The unknown function is represented as $A(\mathbf{x}; V) = s(\mathcal{N}(\mathbf{x}; V)) \times 9 + 3$, where N_f is a fully connected neural network with 2 hidden layers and width 64, and s is the sigmoid activation function (i.e., $s(u) = 1/(1 + \exp(-u))$). The transformation is a smoothed approximation of the piece-wise constant function. For BiLO, the neural net-

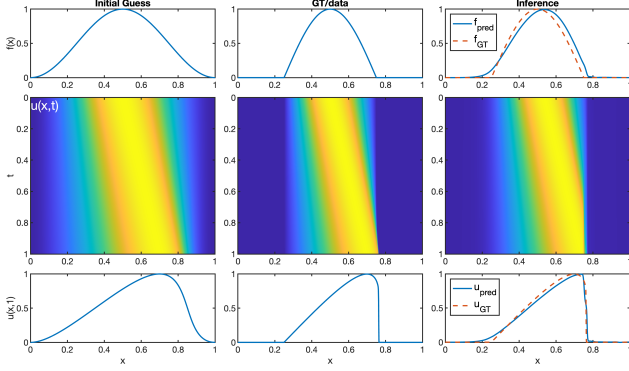


Figure 17: Example 2 of inferring the initial condition of the Burger’s equation.

work is represented as $u(\mathbf{x}, z) = N_u(\mathbf{x}, z; W)\mathbf{x}_1(1 - \mathbf{x}_1)\mathbf{x}_2(1 - \mathbf{x}_2)$, where N_u is a fully connected neural network with 2 hidden layers and width 128, and z is our auxiliary variable such that $z = A(\mathbf{x}; V)$.

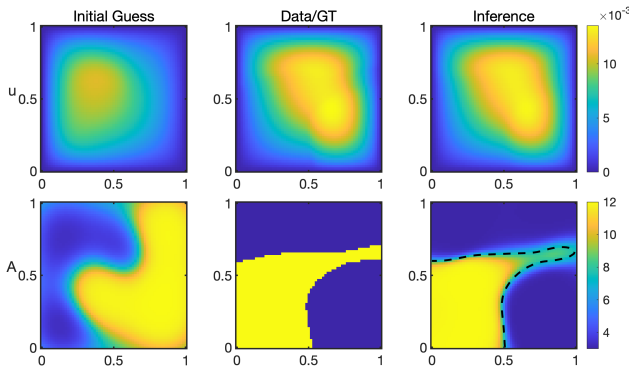


Figure 18: Example 2 of inferring the variable diffusion coefficient. The relative l2 error of u_{NN} against u_{GT} is 1.7%. The thresholded (at the dashed line) inferred diffusion coefficient has classification accuracy of 96%

E. Computational Cost

Compared with PINN, BiLO involve computing a higher order derivative term in the residual-gradient loss. This increases the memory cost and computation time per step. However, as shown in Fig. 8, BiLO might require fewer iterations to achieve certain accuracy of the parameters.

In Table. 6, we show the seconds-per-step and the maximum memory allocation of 1 run of BiLO and PINN for the various problems. The seconds per step is computed by total training time divided by the number of steps. The maximum memory allocation is the peak memory usage during the training. For for all the experiments, we use Quadro RTX 8000 GPU. We note that the measured seconds-per-step is not subject to rigorous control as the GPU is shared

with other users and many runs are performed simultaneously. Detailed study of the computational efficiency of BiLO will be left for future work.

Table 6: Example of computational cost of BiLO and PINN and their ratio for various problems.

Problem	Metric	BiLO	PINN
Fisher-KPP	sec-per-step	0.074	0.045
	max-mem-alloc	200.3	65.1
1D Poisson	sec-per-step	0.064	0.037
	max-mem-alloc	23	20
Heat	sec-per-step	0.070	0.045
	max-mem-alloc	210	109

It is not straightforward to comparing the computational cost with Neural operators. Neural operators can be very fast in the inference stage (solving inverse problem). However, they have significant overhead, which involve preparing the training data, that is, solve the PDE numerically for a large collection of parameters, and pre-train the neural network. The overall cost might be favorable in the many-query settings. However, if we aim to solve the inverse problem once, the total computational cost might not be favorable.

F. Comparison with BPN

In PINN and BPN (Hao et al., 2023), the PDE solution is represented by a neural network $u(x; W)$. Notice that Θ is not an input to the neural network. In both PINN and BPN, the data loss is given by

$$L_{data}(W) = \frac{1}{N} \sum_i (u(x_i; W) - \hat{u}_i)^2$$

and enforce the PDE constraints by minimizing the residual loss.

$$L_{res}(W, \Theta) = \frac{1}{N} \sum_i F(D^k u(x_i; W), \dots, u(x_i; W), \Theta)^2.$$

Motivated by the same concern about the trade-off between the data loss and the PDE loss in a penalty-like formulation in PINN. In BPN, the residual loss is separate from the data loss, leading to the bilevel optimization problem

$$\begin{aligned} & \min_{\Theta} L_{data}(W^*(\Theta)) \\ \text{s.t. } & W^*(\Theta) = \arg \min_W L_{res}(W, \Theta). \end{aligned}$$

Notice that L_{data} depends on Θ in directly through the minimizer of lower level problem. The gradient of the data

loss with respect to the PDE parameters is given by the chain rule

$$\frac{dL_{data}}{d\Theta} = \frac{dL_{data}(W^*(\Theta))}{dW} \frac{dW^*(\Theta)}{d\Theta},$$

where the hypergradient is given by

$$\frac{dW^*(\Theta)}{d\Theta} = - \left[\frac{\partial^2 L_{res}}{\partial W \partial W^T} \right]^{-1} \cdot \frac{\partial^2 L_{res}}{\partial W \partial \Theta^T}.$$

Broyden’s method (Broyden, 1965) is used to compute the hyper-gradient, which is based on the low-rank approximation of the inverse Hessian. In BPN, the bilevel optimization problem is solved iteratively. At each step, gradient descent is performed at the lower level for a fixed number of iterations, N_f . Following this, the hypergradient is computed using Broyden’s method, which requires r iterations to approximate the inverse vector-Hessian product. This hypergradient is then used to perform a single step of gradient descent at the upper level.

The BiLO approach differs significantly. Instead of representing the PDE solution, BiLO represents the local PDE operator, leading to a different lower level problem that includes the residual-gradient loss. In addition, as the local PDE operator includes Θ as an input, the data loss depends on the PDE parameters directly:

$$L_{data}(W, \Theta) = \frac{1}{N} \sum_i (u(x_i, \Theta; W) - \hat{u}_i)^2.$$

This enables direct computation of gradients for L_{data} with respect to Θ , eliminating the need for specialized algorithms to approximate the hypergradient. The residual-gradient loss also ensures that this direction is a descent direction. This formulation also allows us to perform simultaneous gradient descent at the upper and lower levels, which is more efficient than the iterative approach in BPN. Our method is specialized for PDE-constrained optimization, leveraging the structure of the PDE constraint for efficiency (see the proposition in Appendix. C). In contrast, BPN adopts a more general bilevel optimization framework, which, while broadly applicable, does not fully exploit the unique characteristics of PDE problems.

To compare BiLO with BPN, we adopted the problem (33) and the setup from Hao et al. (2023), using the same residual points (64), neural network architecture (4 hidden layers with 50 units), upper-level optimizer (Adam with learning rate 0.05), lower-level optimizer (Adam with learning rate 0.001), and initial guess ($\theta_0 = 0, \theta_1 = 1$). Both methods included 1000 pretraining steps to approximate the PDE solution at initial parameters. In BPN, 64 lower iterations are performed for each upper iteration, with 32 Broyden iterations to compute the hypergradient. By contrast, BiLO performs simultaneous gradient descent at the

upper and lower levels, where each iteration updates both levels concurrently.

$$\begin{aligned} \min_{\theta_0, \theta_1} J &= \int_0^1 (y - x^2)^2 dx \\ \text{s.t. } \frac{d^2 y}{dx^2} &= 2, \quad y(0) = \theta_0, \quad y(1) = \theta_1 \end{aligned} \quad (33)$$

Figure 19 presents the loss and the error of the PDE parameters for both methods versus the number of lower-level iterations. BiLO achieves a parameter error below 0.01 in fewer than 80 iterations and just 6.4 seconds, while BPN requires 27 upper iterations (1728 lower iterations) and 231 seconds to reach the same accuracy. While this highlights BiLO’s efficiency, we note that both methods may benefit from further hyperparameter tuning, and the comparison is made under the settings reported in (Hao et al., 2023).

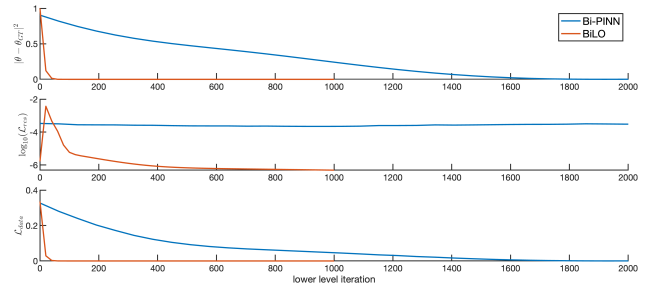


Figure 19: Comparison of BPN and BiLO methods. x-axis is the number of lower level optimization steps. Top: Parameter error $\|\theta - \theta_{GT}\|^2$ versus iterations. Middle: PDE loss $\log_{10}(\mathcal{L}_{res})$. Bottom: Data loss \mathcal{L}_{data} .